Naval Research Laboratory
Washington, DC 20375-5320

NRL/8230/MR—2022/1

Advancing Robotics through Hydraulic Efficiency and Energy Regulation: Program Summary

LOGAN T. WILLIAMS

JOSEPH T. HAYS

DAN S. TABATABAI

Dynamics and Control Systems Branch
Spacecraft Engineering Division

April 29, 2022

REPORT DOCUMENTATION PAGE

Form Approved
OMB No. 0704-0188

1. REPORT DATE *(DD-MM-YYYY)*	**2. REPORT TYPE**	**3. DATES COVERED** *(From - To)*
29-04-2022	NRL Memorandum Report	10-31-2019 – 12-28-2021

4. TITLE AND SUBTITLE

Advancing Robotics Through Hydraulic Efficiency and Energy Regulation: Program Summary

5a. CONTRACT NUMBER

5b. GRANT NUMBER

5c. PROGRAM ELEMENT NUMBER

6. AUTHOR(S)

Logan T. Williams, Joseph T. Hays, and Daniel S. Tabatabai

5d. PROJECT NUMBER

5e. TASK NUMBER

5f. WORK UNIT NUMBER
6B24

7. PERFORMING ORGANIZATION NAME(S) AND ADDRESS(ES)

Naval Research Laboratory
4555 Overlook Avenue, SW
Washington, DC 20375-5320

8. PERFORMING ORGANIZATION REPORT NUMBER

NRL/8230/MR--2022/1

9. SPONSORING / MONITORING AGENCY NAME(S) AND ADDRESS(ES)

Naval Research Laboratory
4555 Overlook Avenue, SW
Washington, DC 20375-5320

10. SPONSOR / MONITOR'S ACRONYM(S)

11. SPONSOR / MONITOR'S REPORT NUMBER(S)

12. DISTRIBUTION / AVAILABILITY STATEMENT

DISTRIBUTION STATEMENT A: Approved for public release; distribution is unlimited.

13. SUPPLEMENTARY NOTES

14. ABSTRACT

This presents a summary of the work conducted on the ARTHuR project and the results obtained and lessons learned.

15. SUBJECT TERMS

Rotary servovalve
Hydraulics
Predictive control

16. SECURITY CLASSIFICATION OF:			**17. LIMITATION OF ABSTRACT**	**18. NUMBER OF PAGES**	**19a. NAME OF RESPONSIBLE PERSON**
a. REPORT	**b. ABSTRACT**	**c. THIS PAGE**			Logan Williams
U	U	U	U	85	**19b. TELEPHONE NUMBER** *(include area code)* (202) 767-9166

This page intentionally left blank.

Closeout Statement

The original plan for the project was a two-pronged approach to address the two primary sources of power loss and inefficiency within a hydraulic quadruped robot: pilot stage loss in the servovalves that control the leg joints, and relief valve loss. The former is the result of using hydraulic actuation within the servovalve to actuate the spool against the induced hydrodynamic forces; the latter is caused by a mismatch between hydraulic fluid supply provided by the pump and fluid demand in the joint actuators. In FY19 development began of an alternative servovalve featuring a rotary servovalve configuration that could balance the hydrodynamic loads on the spool and reduce actuation requirements. Central to this effort was the ability to produce complex internal passages within the valve housing with small-scale, precise, and consistent cross-sections. Collaboration with Code 7165 resulted in preliminary valve housing and spool designs fabricated using additive manufacturing, as well as establishing guidelines for the interior passage design to ensure the desired cross sections with quasi-linear orifice area expansion as a function of spool position. Also in FY19, work on model predictive control (MPC) algorithms began for use in creating a predictive horizon for quadruped fluid requirement modeling.

In FY20 a test-bench setup to characterize the fluid loads on the rotary spool was built; the purpose of this platform was to validate analytical models for spool loading as a function of operating conditions and spool position. However, the onset of the Covid-19 pandemic severely limited access to the laboratory, resulting in all efforts redirected to the hydraulic supply control effort, which could be conducted remotely. A simulation of the quadruped's hydraulic powertrain was created using a combination of analytical models and empirical performance evaluation of the components of the modeled hardware (the quadruped from the MeRLIn program). The MPC work progressed and was generalized to allow utilization by other programs (WISARD, NEMO, etc.) in addition to ARTHuR's use-case.

In FY21 the powertrain simulation and MPC framework was combined with the kinematic simulation package Mujoco and the locomotion control software from the MeRLIn program to create a full-system simulation of the quadruped. The purpose of this simulation is to quantify the impact of the powertrain control scheme (specifically, controlling the speed of the motor powering the hydraulic pump) on the fluid loss through the relief valve, and thus power loss, as the quadruped locomotes. One of the research goals was to ascertain the feasibility of using machine learning algorithms to train a control scheme in simulation. However, it was found that commercial kinematic simulation packages of the type used utilize fixed-time-step integrators, which are incompatibile with variable time-step solvers used in "stiff" simulations, such as hydraulics. Stable simulation of the combined system in a fixed-time-step integrator requires time steps less than a microsecond, resulting in excessively long simulation times that make machine learning currently infeasible. Modification to kinematic simulation packages will be required for further work.

This page intentionally left blank.

Table of Contents

1.0 Introduction

1.1 Description

Advancing Robotics Through Hydraulic Efficiency and Energy Regulation (ARTHuR) was designed to improve the operating time of a battery-powered robotic quadruped by addressing the two primary sources of power loss: pilot loss in the servo valves and relief valve loss. The former is the result of using hydraulic actuation within the servo valve to actuate the spool against the induced hydrodynamic forces; the latter is caused by a mismatch between hydraulic fluid supply provided by the pump and fluid demand in the joint actuators. The goal of this project was to address both issues in a two-pronged approach: to create a rotary valve configuration that balanced the loading on the spool, thereby reducing actuation requirements; to develop a predictive control scheme to regulate the prime mover of the hydraulic power train to minimize excess fluid generation while maintaining the minimum required fluid pressure for optimum locomotion.

1.2 Scope

This document summarizes the work done on the program, including such topics as the:

- Motivation for the work
- Preliminary formulation for the rotary valve
- Investigations into methods of fabrication of the valve components
- Predictive control scheme formulation
- Development of a cross-platform simulation of a quadruped for control testing\
- Lessons learned from the work

1.3 Purpose

This document serves to document work done on the ARTHuR project, the lessons learned, and how elements of this work have transitioned to aid other programs.

Manuscript approved April 27, 2022.

2.0 Motivation

Recent testing of ground robotic systems in field exercises demonstrated that large quadrupeds do not match the needs of the warfighter. Ground troops do not want a mechanical pack mule that is loud and gives away their position, but instead would prefer a smaller, quieter system capable of running a point or flanking position on patrol for early warning and reconnaissance. The Mesoscale Robotic Locomotion Initiative (MeRLIn) began in FY2015 to investigate miniature hydraulics for a small, quiet, and agile quadruped that could provide additional battlefield awareness to the warfighter. The MeRLIn program has developed the hardware and software required for a first generation quadruped, called "Butch," for control algorithm testing, and by the end of the program will develop a second generation unit called "Scout"; these investments will be available to the ARTHuR program as research platforms. The MeRLIn program realized that internal combustion engines are not conducive to warfighter stealth, and that battery-powered operation is required. Additionally, MeRLIn revealed several technological challenges with commercially available hardware that cause significant power loss in hydraulic robotic systems, and thus restrict the mission duration to impractical levels. Overcoming these challenges will be the focus of the research under the ARTHuR program.

Experience in the MeRLIn program has revealed that the powertrain has several mechanisms for loss in both the design of components and their operation. The prime mover, a brushless DC motor (BLDC), has losses through the motor windings, iron losses in the stator, and power factor losses between the electric commutator (EC) and the battery. The hydraulic pump can contribute to power loss by leaking fluid back across the pump as well as frictional and viscous losses. The pressure of the supplied hydraulic fluid is regulated by a relief valve, which dumps all excess fluid to tank, converting the energy to waste heat. The numerous servo valves that control the leg actuators each contain an electromechanically piloted hydraulic stage that actuates the valve spool; this pilot stage constantly drains precious high-pressure hydraulic fluid back to the tank. Fluid that is not leaked through the valves or passed through the relief valve is available to power the actuators providing useful work; all other power is dissipated as waste heat. A conceptual schematic of the drive train is shown below in Figure 2-1.

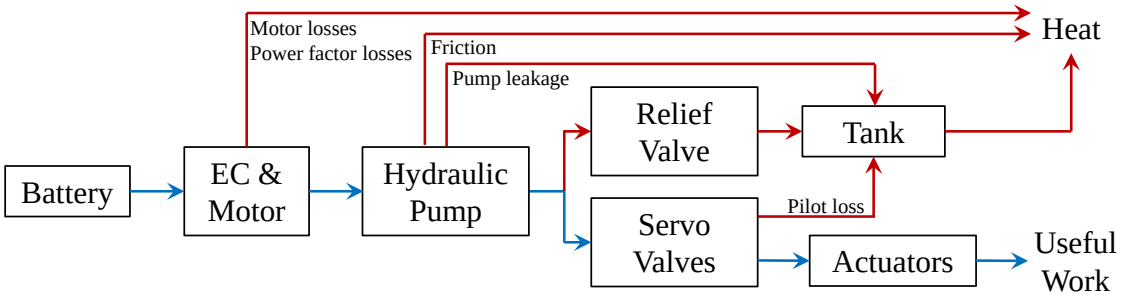

Figure 2-1. Conceptual schematic of a hydraulic system powertrain and associated losses.

To illustrate the power-loss issue, the MeRLIn program Butch prototype system was evaluated with component performance data from each component of the powertrain. Power train losses are multiplicative – each efficiency loss creates additional work each preceding stage. As shown in Figure 2-2, the cascade of power losses results in a total system efficiency of only 5%. Assuming an average velocity of 1.4 m/s (average human walking speed) and a cost of transport equivalent to current quadruped systems, a 10 kg robot with 2 kg of batteries would only have 8 minutes of operating time. There is little room for improvement within the pump or motor itself, as these technologies are mature and already achieve 80-85% efficiency. Pilot valve leakage and relief valve losses, however, remain an untapped potential for systemic improvement. A new valve concept developed under ARTHuR is clearly

needed. Additionally, ARTHuR will build on existing progress by developing advanced predictive algorithms to actively control the motor speed and allowing the pump created under MeRLIn to operate with reduced relief valve waste. By doing so, the required input electrical power of a hydraulic system can be decreased to the point that current battery storage capacity is sufficient to enable useful mission durations.

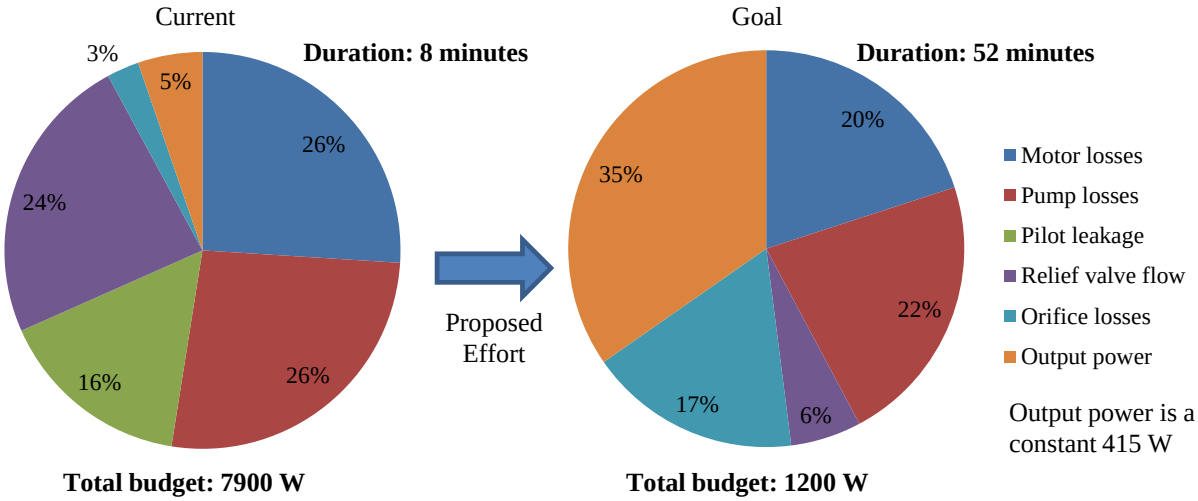

Figure 2-2. Powertrain budget for a 10 kg robot. ARTHuR eliminates pilot leakage (green) and reduces relief valve flow (purple) to reduce total powertrain power draw, and dramatically extend mission duration.

As previously mentioned, standard commercial components and industry operational practices are ill-suited for small energy-limited platforms. In order to control high pressure fluid flows around the controlling surface, called the spool, the valves require relatively large actuation forces. The two most common methods in commercial valves are a linear motor or an electromechanically piloted hydraulic actuator. While the use of high-pressure hydraulic fluid results in smaller and lighter actuation stages than a linear motors, it constantly drains fluid (and thus power) from the system. As an example, the current servo valves used in Butch, the Moog E024, are designed for Formula 1 race cars. They have high power throughput, low mass (92 g), and small form factor, but 0.08 gpm pilot loss per valve. For the rated pressure of 3000 psi, this results approximately 100 W lost per valve; a small expense for a 700 kW Formula 1 racing engine, but severe for the power budget of a few kilowatts for a battery-powered system. Alternatively, the Moog E242 micro direct-drive valve couples the same valve to a linear motor, yielding identical performance without pilot loss, but a valve mass of 187 g. While the extra 95 g per valve is small for a 700 kg car, it is a tall order for a 5-10 kg quadruped. What is needed is a servo valve that can achieve fast actuation with neither pilot fluid loss nor a heavy linear motor. As will be discussed in the technical approach, ARTHuR invents such a valve by moving from a linear spool architecture to a rotary spool concept that is revolutionary at this small scale.

High efficiency pressure regulation of the hydraulic system is another challenge that ARTHuR will solve. Common hydraulic powertrains use fixed displacement pumps driven by constant-speed motors, where the pump feeds hydraulic fluid at a rate proportional to the drive speed of the pump. To avoid over-pressurizing the system during low flow operations, a relief valve vents excess fluid to the reservoir tank. For dynamic systems that would observe large changes in the powertrain demands, such as an autonomous robotic system, this results in significant and nearly constant power loss through the relief valve. The traditional industrial alternative to reduce fluid waste is to use a variable-displacement pump, such as an axial piston swash plate pump, that adjusts the displacement of the pump by a pressure-compensated piston to create a feedback loop between system pressure and displacement. However, it is difficult to reliably miniaturize such systems to the extent required for small-scale robotics. Another

approach is to utilize a fixed-displacement pump, which can be readily miniaturized, in conjunction with a variable-speed motor. While this provides a more energy-efficient solution, preliminary modeling of dynamic speed control has shown that a simple pressure regulation control scheme creates a non-negligible bandwidth lag between system demand (legged locomotion and actuation), and powertrain response. The ARTHuR program seeks to solve this problem and maintain system responsiveness by shifting powertrain control from passive pressure regulation to a predictive scheme based on legged locomotion demand and actuator drive commands. Current research in the literature remains in the realm of PID pressure control for fluid supply, leaving an opportunity for NRL to leverage the assets and expertise developed under MeRLIn to delve into a new realm of predictive hydraulic system control that can extend mission durations without compromising system responsiveness or locomotive capability.

3.0 Rotary Valve Design Concept

The baseline servo valve to which any alternative design will be evaluated against is the spool valve. The spool valve is a relatively well studied and understood design which uses the linear motion of a flanged spool to dictate fluid flow pathways. Sealing is accomplished through the narrow clearance between the spool flanges (called lands) and the inner diameter of the valve housing. Two design challenges associated with spool valves are: compensating for the flow forces on the spool, and providing sufficient linear motion in a compact form factor. The rotary valve design attempts to circumvent these two challenges by transforming the issue from one of linear spool actuation, to one of rotary cylinder control.

3.1 Design Overview

The basic premise of the design is to take a four-way valve and instead of using a linear actuator and spool to route the fluid, a rotating cylinder with internal passages inset of a valve body with a matching set of interior passageways is used. The valve state can then be changed between any of the three permutations for the valve by simply rotating the cylinder a set amount. More precise control of the valve can be achieved by fine tuning the amount the cylinder is rotated. In these types of valves there are four ports to the external system, two for the system pressure and return, and two for the actuator connected to the valve, designated P, R, A, and B, respectively. Fluid can be routed between these ports by passing through the internal passageways of the valve body into the rotary cylinder, and back to the valve body in the appropriate passageway to the port of choice. A closed valve state can be achieved by rotating the cylinder such that no aperture of the valve body is exposed. A conceptual CAD rendering is shown in Figure 3-1.

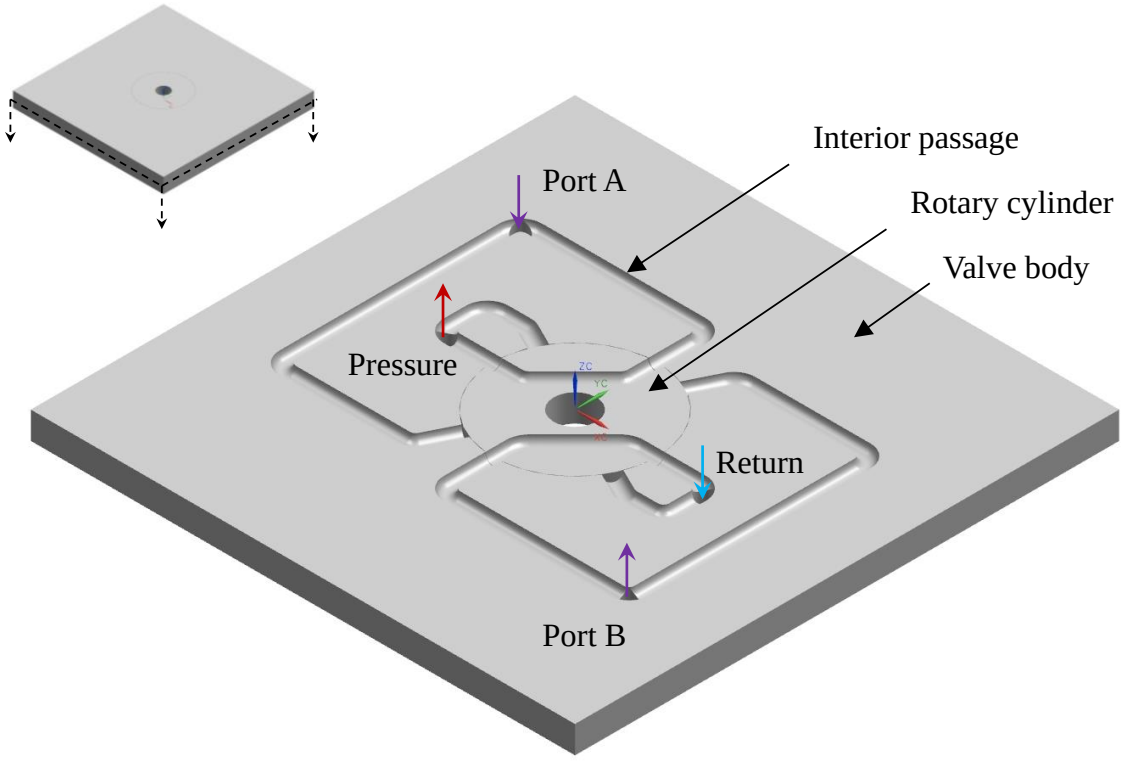

Figure 3-1. Cross section of rotary valve concept.

Initially, the valve body only requires one orifice per port to the cylinder, while the cylinder would consist of two interior passages to connect any two ports. However, such an arrangement would require a 90° rotation to change between the two open configurations (e.g. going from P-A to P-B). Since servo valves are often used in applications that require fast response times, it would be beneficial to minimize the angular displacement required to change valve state. Thus, there are two apertures in the valve body for each port such that a small rotation is sufficient to change between valve states. In the geometry of the conceptual CAD design, transitioning between the two open states can be achieved with a rotation of approximately 26°, shown in Figure 3-2.

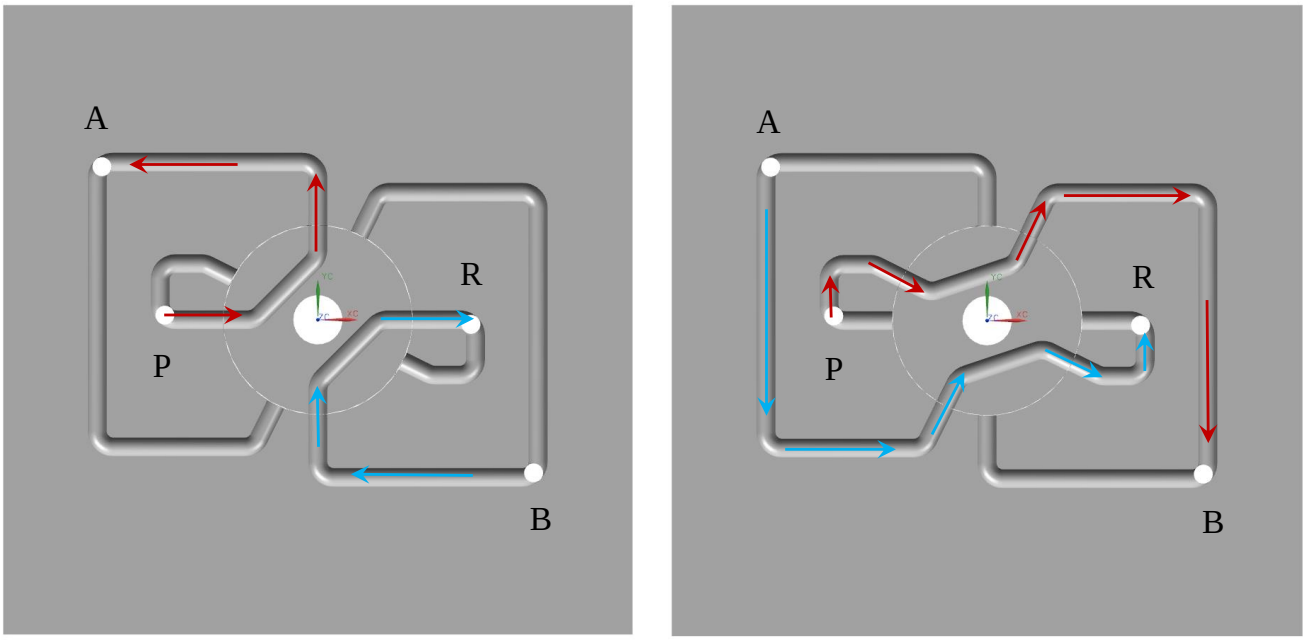

Figure 3-2. Valve states using multiple internal passages. State 1 (*left*) with A connected to pressure and B to return; state 2 (*right*) with B connected to pressure and A to return.

3.2 Hydrodynamic Loading

The feasibility of the design and its appeal over the standard spool valve relies on the design fulfilling the requirements of the valve with a minimal load placed on the actuator. Following the methodology outlined by Manring, the various loads placed on the cylinder in the course of operation are estimated. These loads include steady loading for both open and closed states, transient flow forces, viscous shear forces in the internal passages, and viscous shear loading of the cylinder rotating against the valve body.

3.2.1 Steady fluid loading

To begin, a control volume can be drawn around the interior passageways of the cylinder, as shown below in Figure 3-3. In this instance, the valve is assumed to be held fully open. Assuming the orientation of fluid ports for State 1 as shown in Figure 3-2, fluid flows in from the pressure at the 9 o'clock position and exits at the 12 o'clock position to port A; likewise, fluid arrives from port B at the 6 o'clock position and exits at the 3 o'clock position to the return line.

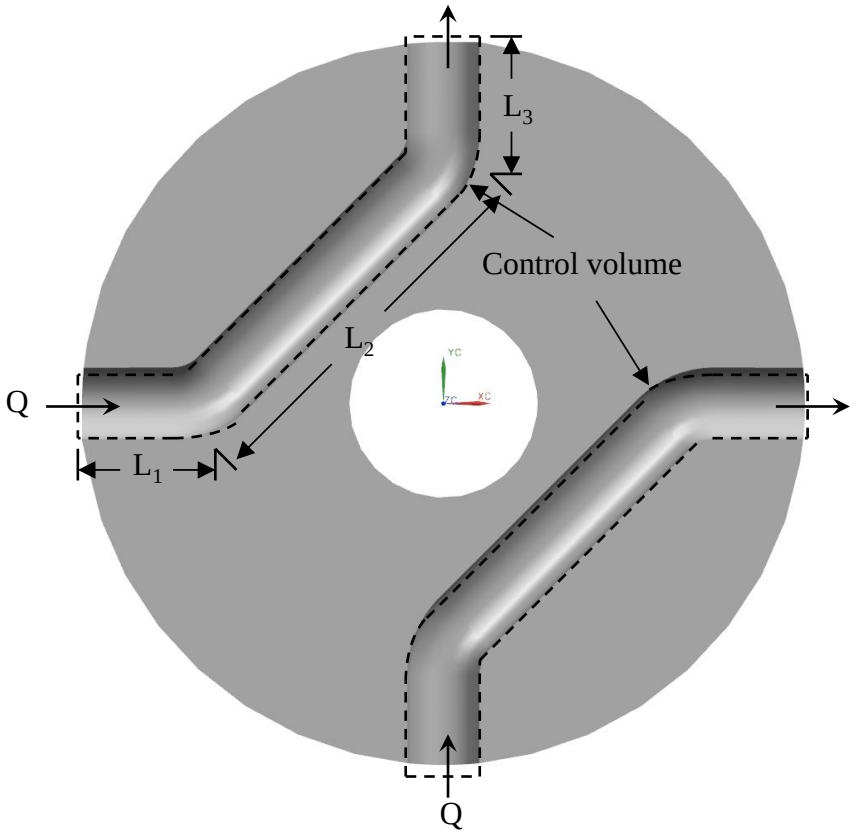

Figure 3-3. Control volume of the static open condition of the valve cylinder.

The forces from the fluid on the boundaries of the control volume are given by the Reynolds transport theorem for momentum,

$$F_M = -\iint_{CS} \rho \vec{u}(\vec{u} \bullet \hat{n}) dA - \frac{\partial}{\partial t} \iiint_{CV} \rho \vec{u} dV - F_{surface} \tag{3.1}$$

where ρ is the density of the fluid, u is the velocity of the fluid, n is the unit vector normal to the control surface, and $F_{surface}$ denotes surface forces within the system, namely viscous shear. It should be noted that the right hand side of Equation (3.1) is negative, since the Reynolds transport theorem describes the force on the fluid, whereas in this case it is the force on the control volume (the valve) that is of interest. The surface integral and the volumetric integral terms can be thought of as a steady and a transient momentum force components, respectively.

$$F_M = -F_s - F_t - F_{surface} \tag{3.2}$$

Taking the steady term first, there are three possible conditions of the valve: fully open, fully closed, and partially open. For the time being, the difference between valve states 1 and 2 is unimportant, as the resulting loads would only differ by an angular displacement. Beginning with the fully open condition and the orientation shown in Figure 3-2, the steady momentum force component can be described in terms of the volumetric flow rate, Q, and the bulk fluid velocity, u.

$$\vec{F}_s = \rho Q\left[\left(-u\hat{i} + u\hat{j}\right) + \left(u\hat{i} - u\hat{j}\right)\right] = 0 \tag{3.3}$$

Thus, as a result of the symmetry of the valve cylinder fluid pathways, for a fully open valve there is no net steady state change in fluid momentum through the cylinder. Even though individual passages experience a change in momentum, it is balanced on the other side of the cylinder.

For the next valve condition, fully closed, there is nominally no fluid flow through the valve, except for any leakage fluid between the ports. For an initial estimate of valve loading, fluid leakage is neglected. In this state, there are two pressure differentials operating on the cylinder: the system pressure drop between ports P and R, and any externally induced pressure from the actuator across A and B (e.g. if the actuator was externally actuated by an outside force). The magnitude of the net load on the cylinder is

$$F_{s,closed} = A_p \sqrt{\left(\Delta p_{PR}\right)^2 + \left(\Delta p_{AB}\right)^2} \tag{3.4}$$

where A_p is the cross sectional area of the passage. This radial load must be taken either by some bearing, or by the cylinder itself acting as a journal bearing. If the latter is the case, this creates an additional torque load to overcome friction in order to open the valve. This torque can be estimated by

$$T_{s,closed} = \mu_s r_c A_p \sqrt{\left(\Delta p_{PR}\right)^2 + \left(\Delta p_{AB}\right)^2} \tag{3.5}$$

where r_c is the radius of the cylinder, and μ_s is the coefficient of static friction; for lubricated metals, this value is generally in the range of 0.1-0.3.

The final valve condition is partially open; in this state the fluid flow is no longer purely radial at the inlets and outlets of the cylinder. Instead, the discharge of fluid through the small aperture of area A_o, formed by a partially open valve creates a fluid jet at an angle to the valve body, φ, as shown in Figure 3-4. The value of this angle is estimated using Von Mises' solution to the problem for a spool valve configuration, which is dependent on the clearance between the cylinder and the valve body, δ_r, and the distance the valve has been opened, x.[1]

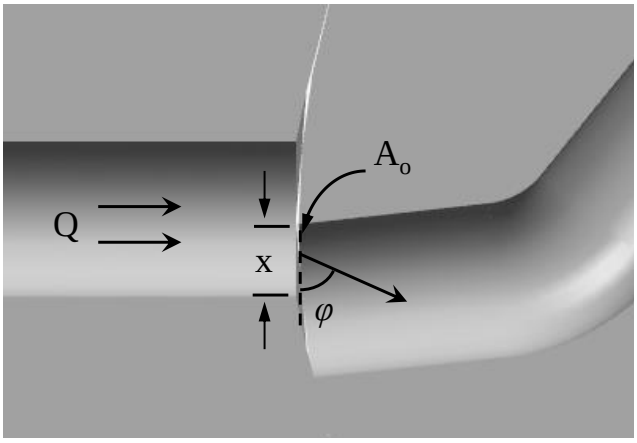

Figure 3-4. Jet geometry for partially opened valve.

$$\frac{x}{\delta_r} = \frac{1+\frac{\pi}{2}\sin\varphi - \ln\left[\tan\left(\frac{\pi-\varphi}{2}\right)\right]\cos\varphi}{1+\frac{\pi}{2}\cos\varphi + \ln\left[\tan\left(\frac{\pi/2-\varphi}{2}\right)\right]\sin\varphi} \tag{3.6}$$

The solution for Equation (3.6) is shown below in Figure 3-5. As can be seen, the jet angle is bounded in the range of approximately 21°-69°. It should be noted that the above equation has no transition to large valve openings where the flow is expected to be largely parallel with the flow passages, i.e. where φ approaches 90°. It is difficult to conceive of a fully opened valve resulting in a jet angle of 69°. Thus, the jet angle is arbitrarily modeled such that when the valve opening is half of the port diameter, the jet angle is calculated as the linear interpolation between 69° and 90°.

$$\varphi = 1.2 + 2\left(\pi/2 - 1.2\right)\left(\xi/d_p - 1/2\right) \qquad [rad] \tag{3.7}$$

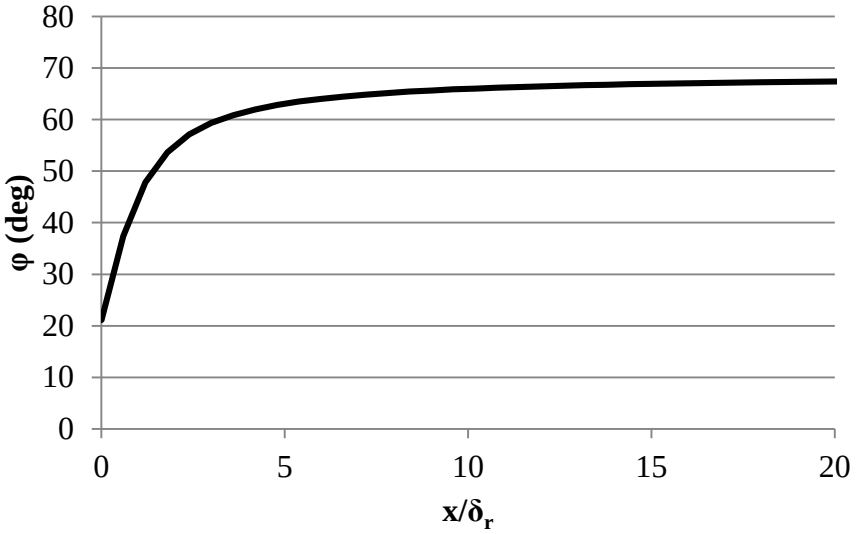

Figure 3-5. Jet angle as a function of the ratio of aperture width to cylinder clearance.

Considering the symmetry of the cylinder passages already observed in the fully open condition, the radial components of the jet momentum forces remain balanced and provide no net force on the cylinder. However, tangential loads impart a net torque on the cylinder which are not balanced, but are instead cumulative. Therefore, tangential jet forces are the item of interest in this condition, given as

$$F_{s,\tan} = \frac{\rho Q^2}{C_c A_o}\cos\varphi \tag{3.8}$$

where C_c is the contraction coefficient. Neglecting fluid compressibility through the aperture, the flow rate through the partially open valve can be defined in terms of the pressure drop across the valve,

$$Q = C_d A_o \sqrt{\frac{2}{\rho}\Delta p} \tag{3.9}$$

where C_d is the discharge coefficient. The discharge coefficient can be defined in relation to the flow contraction coefficient and the flow coefficient, C_v.[2]

$$C_d = C_c C_v \tag{3.10}$$

Substituting Equations (3.9) and (3.10) into Equation (3.8) yields the tangential force on the cylinder from a single jet.

$$F_{s,\tan} = 2C_d C_v A_o \Delta p \cos\varphi \tag{3.11}$$

The area of the aperture as a function of the aperture width varies with the geometry of the fluid passage. For a square passage of width *w*, the area is

$$A_o(x) = wx$$

while for a passage with a circular cross section of diameter *d* is

$$A_o(x) = \frac{\pi}{8}d^2 + \left(x - \frac{d}{2}\right)\sqrt{(d-x)x} + \frac{d^2}{4}\arcsin\left(2\frac{x}{d} - 1\right)$$

Therefore the tangential load on the cylinder will vary slightly with the geometry of the passage.

3.2.2 Transient fluid loading

Assuming that density and flow area is constant with respect to time, the transient momentum force component can be defined as

$$F_t = \iiint_{CV} \rho \frac{\partial \vec{u}}{\partial t} dV$$

$$F_t = \int_s \rho \frac{\partial \vec{u}}{\partial t} A_c ds$$

where *s* corresponds to a path line along the passageway in the cylinder. Again using the geometry in Figure 3-3, the transient force can be described in terms of the change in volumetric flow rate.

$$\vec{F}_t = -2\left(\rho L_1 \frac{\partial Q}{\partial t} + \frac{1}{\sqrt{2}}\rho L_2 \frac{\partial Q}{\partial t}\right)\hat{i} - 2\left(\rho L_3 \frac{\partial Q}{\partial t} + \frac{1}{\sqrt{2}}\rho L_2 \frac{\partial Q}{\partial t}\right)\hat{j}$$

Assuming the radial cylinder passage lengths are equal, ($L_1 = L_3$), the magnitude of the transient force can be simplified to

$$F_t = -2\rho \frac{\partial Q}{\partial t}\left(\sqrt{2}L_1 + L_2\right) \tag{3.12}$$

This load is purely radial, as the tangential components along L_2 are balanced by cylinder symmetry.

3.2.3 Shear loading

Another component of fluid loading on the cylinder is the impact of viscous drag on the fluid by the cylinder. This viscous force is defined as

$$\vec{F}_\tau = \mu \left.\frac{\partial \vec{u}}{\partial r}\right|_{r_p} A_{surface} \tag{3.13}$$

where $\partial u/\partial r$ denotes the velocity gradient of the fluid in the direction normal to the flow, and $A_{surface}$ is the surface area wetted by the fluid. Breaking the flow passage into the three segments shown in Figure 3-3, Equation (3.13) can be written as

$$\vec{F}_\tau = \sum_i \mu \pi d_h L_i \frac{\partial \vec{u}}{\partial r} \tag{3.14}$$

where d_h is the hydraulic diameter of the passage. Using the Navier-Stokes equations and assuming steady, fully developed flow, the fluid velocity gradient at the wall can be approximated as

$$\left.\frac{\partial u}{\partial r}\right|_{r_p} = \frac{1}{4}\mu d_h \frac{\Delta p_i}{L_i}$$

where Δp_i is the pressure drop through the i^{th} leg of the fluid passage. Recognizing that the shear loading has the same geometry as the transient fluid loading, the magnitude of the force can be written similarly.

$$F_\tau = \frac{1}{4}\mu^2 \pi d_h^2 \frac{\Delta p_f}{2L_1 + L_2}\left(\sqrt{2}L_1 + L_2\right) \tag{3.15}$$

The frictional pressure drop through the entire cylinder passage, Δp_f can be described in terms of the volumetric flow rate using the Darcy-Weisbach equation,

$$\Delta p_f = f \frac{L}{d_h} \frac{\rho u^2}{2}$$

where *f* is the Darcy friction factor, resulting in the shear load on the cylinder from interior fluid flow.

$$F_\tau = \frac{\mu^2 f \rho Q^2}{2 d_h} \left(\sqrt{2} L_1 + L_2 \right) \tag{3.16}$$

Another source of shear load on the cylinder is from the viscous drag from fluid between the cylinder and the valve body. For a reasonably small radial clearance between the cylinder and the valve body (which would be required to reduce leakage), the cylindrical geometry can be approximated as a linear Couette flow. From a 2-D Navier-Stokes formulation, assuming fully developed (but not steady state), the momentum conservation equation in the *y*-direction (normal to the flow) reduces to

$$\frac{\partial u}{\partial t} = \frac{\mu}{\rho} \frac{\partial^2 u}{\partial y^2}$$

Approximating the time rate of change in velocity in terms of the angular acceleration, discussed in the next subsection,

$$\frac{\partial u}{\partial t} \approx \frac{r_c \omega}{t_{res}} \approx \frac{1}{2} r_c \alpha$$

while the *y*-axis momentum equation can be simplified to the following.

$$\frac{\partial^2 u}{\partial y^2} = \frac{\rho r_c \alpha}{2 \mu}$$

With the boundary conditions that $u = 0$ at $r = r_c$, and $u = 0$ at $r = r_c + \delta_r$, the velocity gradient at the wall is found to be

$$\left. \frac{\partial u}{\partial y} \right|_{y=0} = \frac{\rho r_c \alpha \delta_r}{4} - \frac{\mu r_c \alpha t_{res}}{2 \delta_r} \tag{3.17}$$

The frictional torque on the cylinder can then be found as

$$T_{vis} = \mu r_c A_{surface} \left. \frac{\partial u}{\partial y} \right|_{y=0}$$

$$T_{vis} = -\pi r_c^3 h \alpha \left(\frac{\rho \delta_r}{2} + \frac{\mu t_{res}}{\delta_r} \right) \tag{3.18}$$

3.2.4 Inertial loading

Due to the nature of the servo valve as a highly transient device, there is the additional consideration for inertial loads. In order for the valve to properly function within a given application, it must be capable of rotating the cylinder rapidly enough to accurately change the valve state within some set response time, t_{res}. The fastest response is where the cylinder is accelerated for half of the time, and decelerated the other half as the cylinder stops at the desired position. Given the angular displacement required from the geometry to change valve states, $\Delta\theta$, the angular acceleration, α, can be estimated as

$$\alpha = \frac{4\Delta\theta}{t_{res}^2} \tag{3.19}$$

The torque required to impart this angular acceleration is given by

$$T = I\alpha \tag{3.20}$$

where I is the moment of inertia of the cylinder, which can be estimated as

$$I = \frac{\pi}{2} \rho_c r_c^4 h \tag{3.21}$$

where ρ_c is the density of the cylinder, and h is the height of the cylinder. Substituting Equations (3.16) and (3.21) into (3.19) yields an estimate for the torque required to overcome inertia.

$$T = 2\pi \rho_c r_c^4 h \frac{\Delta\theta}{t_{res}^2} \tag{3.22}$$

3.2.5 Pressure loading

The final source of loading considered is frictional torque between the cylinder and the valve housing due to radial forces caused by pressure imbalances. When the valve is fully open, the flow passages of the housing and the cylinder are in alignment and there is no surface for the pressure to act on. When the valve is only partially open, however, part of the cylinder is exposed to each port in the housing. Due to the difference in fluid pressure at each port, this creates a radial force on the cylinder. In the absence of a bearing or some other constraint on the cylinder, this radial force will press the cylinder against the valve housing. During actuation of the valve this will lead to rubbing friction and an added

torque on the shaft. The radial load is the vector sum of two pressure differentials which are orthogonal, so the magnitude of the net radial load is

$$F_{r,p} = \sqrt{A_c^2\left(\left(p_S - p_R\right)^2 + \left(p_A - p_B\right)^2\right)} \tag{3.23}$$

where A_c is the "closed" area of the cylinder, defined in terms of the open area of the port.

$$A_c = A_p - A_o$$

The torque on the cylinder can then be calculated in terms of the radial load, which is assumed to be equal to the normal force on the cylinder.

$$T_f = \mu_k r_c F_r \tag{3.24}$$

The above analysis applies to the valve ports that constitute the flow connections through the rotary cylinder. In addition to these four "active" ports are four "inactive" ports at any given time, which correspond to the redundant flow passages used to reduce the rotary stroke. The inactive ports allow a steady pressure differential to act on the cylinder at all valve states; as the inactive ports become active during actuation, the previously active ports become inactive (assuming the valve is not undercut). The net result is four pressure gradients acting on the cylinder at any given time, the vector sum of which is the net radial load that determines the normal force on the cylinder used for frictional power loss. This net radial force can be calculated in terms of the forces of the open ports, F_p, the forces of the inactive or closed ports, F_c, and the angle between adjacent ports, θ_{pp}.

$$\vec{F}_{r,net} = \left(F_{p1} + F_{c1}\cos\theta_{pp} + F_{c2}\sin\theta_{pp}\right)\hat{i} + \left(F_{p2} + F_{c1}\sin\theta_{pp} + F_{c2}\cos\theta_{pp}\right)\hat{j} \tag{3.25}$$

In Equation (3.25), the subscripts 1 and 2 denote the supply/return and A/B port pressure differentials, respectively. The net radial force can be further reduced by modifying the interior flow passages of the valve body such that the active and inactive ports are in opposition, balancing the radial load somewhat. This requires more extensive internal routing of the flow passages for the supply and return ports, but reduces frictional loss.

3.3 Unequal Flow Condition

Thus far it has been assumed that the flow rate through the valve is uniform. This assumption requires two conditions: that internal leakage is zero, and that fluid flow out of port A is the same as the flow in through port B. The first, negligible internal leakage, while likely not completely accurate, does not strongly affect the load on the cylinder. The other condition, flow balance, is at the heart of the rotary valve concept of load balancing. In actual practice, a valve is not an isolated unit, but is instead a component of a larger system. The most common use, and the one in mind for this effort, is the use of the valve to control a hydraulic actuator, namely a double-acting cylinder. For double acting cylinders, the presence of a shaft connecting the piston to the load creates an area difference between one side of

the piston and the other, which in turn means that when the piston is in motion the flow rates in and out of the cylinder differ. A conceptual illustration of this is shown in Figure 3-6.

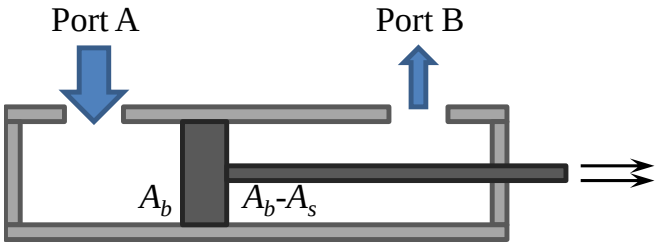

Figure 3-6. Variable flow in double acting cylinder.

The cylinder can be characterized by a bore radius, r_b, and a shaft radius, r_s, with the piston moving at a velocity of u. The volumetric flow rate into the cylinder from port A is equal to the product of the cross sectional area of the cylinder bore, A_b, and the piston speed u.

$$Q_A = A_b u \tag{3.26}$$

In the same way, the volumetric flow rate out of the cylinder to port B is in terms of the bore area and shaft area, A_s.

$$Q_B = \left(A_b - A_s\right)u \tag{3.27}$$

The flow rates can be related by the ratio of the shaft area to the bore area, AR.

$$Q_B = Q_A \frac{A_b - A_s}{A_b} = Q_A\left(1 - AR\right) \tag{3.28}$$

The steady momentum force loading on the cylinder then becomes

$$\sum F_{s,x} = \frac{\rho}{A_o}\left[Q_S^2 \sin\theta - Q_A^2 \cos\theta + Q_B^2 \cos\theta - Q_R^2 \sin\theta\right]$$

$$\sum F_{s,y} = \frac{\rho}{A_o}\left[-Q_S^2 \cos\theta - Q_A^2 \sin\theta + Q_B^2 \sin\theta + Q_R^2 \cos\theta\right]$$

$$\sum M_s = \frac{r_c \rho}{A_o}\left[-Q_S^2 \cos\theta - Q_A^2 \cos\theta - Q_B^2 \cos\theta - Q_R^2 \cos\theta\right]$$

where M denotes the moments on the cylinder. Assuming no internal leakage, the flow rate through the supply port is the same as through the A port; likewise with port B and the return port. The steady momentum force loads on the cylinder can then be simplified further.

$$\sum F_{s,x} = \frac{\rho}{A_o}\left(Q_A^2 - Q_B^2\right)\left(\sin\theta - \cos\theta\right) \tag{3.29}$$

$$\sum F_{s,y} = -\frac{\rho}{A_o}\left(Q_A^2 - Q_B^2\right)\left(\sin\theta + \cos\theta\right) \tag{3.30}$$

$$\sum M_s = -\frac{2r_c\rho}{A_o}\left(Q_A^2 + Q_B^2\right)\cos\theta \tag{3.31}$$

3.4 System Solution Determination

The equations defined thus far outline the force loads on the valve cylinder and are dependent on the flow rates through the valve. However, a set flow rate is not necessarily known, but rather the pressure across the valve/actuator system. Thus the flow rates through the valve must be calculated as a function of the pressure drop across the system and the valve state. This can be done by examining each of the pressure losses through the valve and calculating the pressure at each junction. The three main kinds of pressure drops in the system are: orifice losses for a partially opened valve, viscous losses through internal passages of the valve, and pressure loss through an actuator against the primary load. For simplicity, the viscous losses through the internal passages of the cylinder can be considered negligible such that each passage in the cylinder can be considered uniform, p_1 for between ports S and A, and p_2 for between ports B and R. This is illustrated below in Figure 3-7. The assumptions used in Section 3.3 still apply, and thus only two component flow rates are considered: Q_A and Q_B.

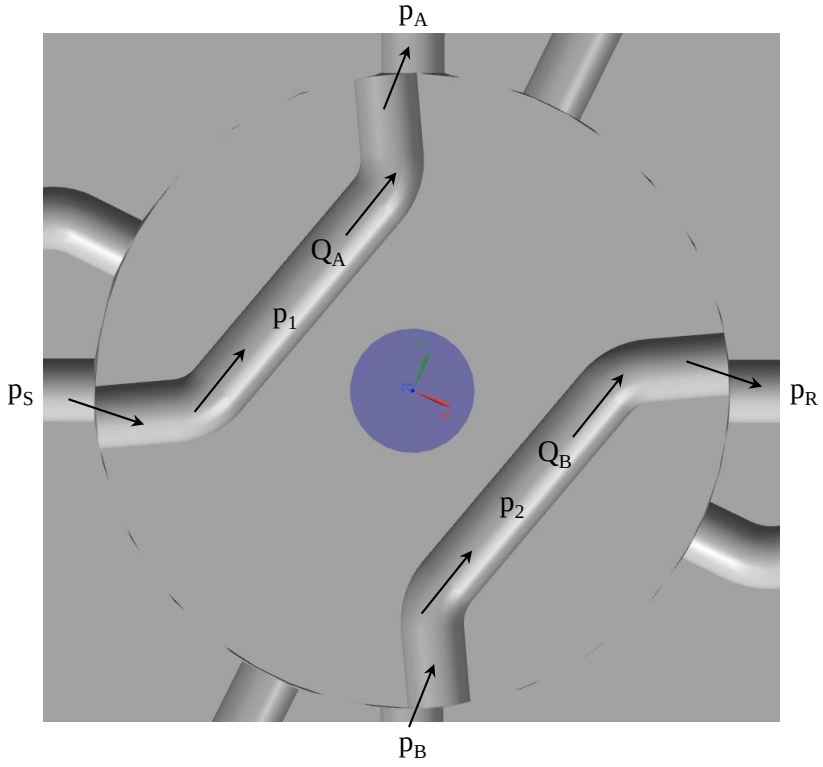

Figure 3-7. Valve pressures and flow rates.

The pressure drop through the orifice of a partially opened valve can be modeled as

$$\Delta p_{orifice} = \frac{\rho Q^2}{2C_d A_o^2}\left(1-\left(\frac{d_{o,h}}{d_p}\right)^4\right)$$

where $d_{o,h}$ is the hydraulic diameter of the orifice, which can be written as follows.

$$d_{o,h} = \frac{2d_p\xi}{d_p+\xi} \tag{3.32}$$

Thus, for a given supply and return pressure, the other pressures in the valve can be written in terms of the component flow rates.

$$p_1 = p_S - \frac{\rho Q_A^2}{2C_d A_o^2}\left(1-\left(\frac{d_{o,h}}{d_p}\right)^4\right) \tag{3.33}$$

$$p_A = p_1 - \frac{\rho Q_A^2}{2C_d A_o^2}\left(1-\left(\frac{d_{o,h}}{d_p}\right)^4\right) \tag{3.34}$$

$$p_2 = p_R + \frac{\rho Q_B^2}{2C_d A_o^2}\left(1-\left(\frac{d_{o,h}}{d_p}\right)^4\right) \tag{3.35}$$

$$p_B = p_2 + \frac{\rho Q_B^2}{2C_d A_o^2}\left(1-\left(\frac{d_{o,h}}{d_p}\right)^4\right) \tag{3.36}$$

If the valve is symmetric such that all four orifices are identical at all valve positions, Equations (3.33) through (3.36) can be written in terms of a common flow constant, K_Q.

$$p_1 = p_S - K_Q Q_A^2 \tag{3.37}$$

$$p_A = p_1 - K_Q Q_A^2 \tag{3.38}$$

$$p_2 = p_R + K_Q Q_B^2 \tag{3.39}$$

$$p_2 = p_R + K_Q Q_B^2 \tag{3.40}$$

$$K_Q = \frac{\rho}{2C_d A_o^2}\left(1-\left(\frac{d_{o,h}}{d_p}\right)^4\right) \tag{3.41}$$

The pressure on the body side of the orifice, what is referred to as p_S or p_A is not exactly what the pressure is from the perspective of the hydraulic system, as there are internal passageways through the valve body to reach the cylinder. The pressure drop due to viscous losses through the internal passages can be modeled as

$$\Delta p_{line} = \frac{128\mu L}{\pi d_p^4} Q$$

where L is the length of the passage. Based on the architecture conceptualized in Figure 3-2, where the line length inside the valve body to the S and R ports is much smaller than the length to the A and B ports, pressure losses from these ports to the cylinder can be neglected. Thus, the pressure at the cylinder from ports S and R is effectively the supply and return pressures of the system, respectively. The system pressure for ports A and B at the exterior of the valve can then be calculated as

$$p_A^* = p_A - K_{LA} Q_B \tag{3.42}$$

$$p_B^* = p_B + K_{LB} Q_B \tag{3.43}$$

where K_{Li} is the flow constant for a given branch, defined below.

$$K_{Li} = \frac{128\mu L_i}{\pi d_p^4} \tag{3.44}$$

The pressures can next be related by assuming that the pressure drop across the load is two thirds of the total system drop (the 1/3-2/3 rule).

$$p_A^* - p_B^* = \frac{2}{3}\left(p_S - p_R\right) \tag{3.45}$$

Substituting Equations (3.37) through (3.43) and Equation (3.28) into Equation (3.45) yields a relation for the primary flow rate as a function of the flow constants and the system pressures.

$$2K_Q\left(1+\left(1-AR\right)^2\right)Q_A^2 + \left(K_{LA} + K_{LB}\left(1-AR\right)\right)Q_A - \frac{1}{3}\left(p_S - p_R\right) = 0$$

Solving the quadratic equation for Q_A yields

$$Q_A = \frac{-\left(K_{LA} + K_{LB}\left(1-AR\right)\right) + \sqrt{\left(K_{LA} + K_{LB}\left(1-AR\right)\right)^2 + \frac{8}{3}K_Q\left(p_S - p_R\right)\left(1+\left(1-AR\right)^2\right)}}{4K_Q\left(1+\left(1-AR\right)^2\right)} \tag{3.46}$$

Once Q_A has been determined, the rest of the system parameters can be calculated. It should be noted that K_Q is a function of the valve opening, ξ, and thus Q_A is not static; the term "flow constant" is a slight misnomer, as K_Q is not constant.

3.5 Case Study

As a quantitative example of the valve concept, a case study was performed based on the CAD model shown in previous figures. The geometric parameters and operating conditions are listed below in Table 1 and Table 2, respectively. Note that $\Delta\theta_{closed}$ corresponds to the angular distance (edge-to-edge) between two adjacent flow passages in the valve body. The coefficient of friction was estimated from journal bearing performance in the mixed-film regime, as this represents the intermittent behavior of the valve action preventing a fully developed lubrication film from forming.

Table 1. Geometric parameters of rotary valve case study.

r_c	0.15 in
h	0.1 in
d_h	0.030 in
δ_r	0.0005 in
L_1, L_3	0.05 in
L_2	0.141 in
$\Delta\theta_{closed}$	12.5°

Table 2. Operating conditions of rotary valve case study

ρ_c	2700 kg/m^3
ρ_f	850 kg/ m^3
μ_f	0.0187 kg/m-s
μ_k	0.05
p_S	2900 psi
p_R	14.5 psi
t_{res}	3 ms

Using the above parameters, the loads on the valve cylinder are calculated and plotted as a function of spool opening below in Figure 3-8. The primary components to cylinder loading are from particular conditions that, strictly speaking, do not occur simultaneously: the pressure differential across a fully closed valve and the flow forces on a partially opened valve. Additionally, the transient momentum force was found to be much less than the radial force on the cylinder from the pressure differential. The three primary components to the torque on the cylinder are: bearing friction of the rotating cylinder, fluid viscosity, and cylinder inertia. Numerical integration of the torque loads on the cylinder yields the

net work required to rotate the cylinder from closed to a given valve position, shown in Figure 3-9. Note that this does not include work required to overcome the inertia of the motor used to drive the valve.

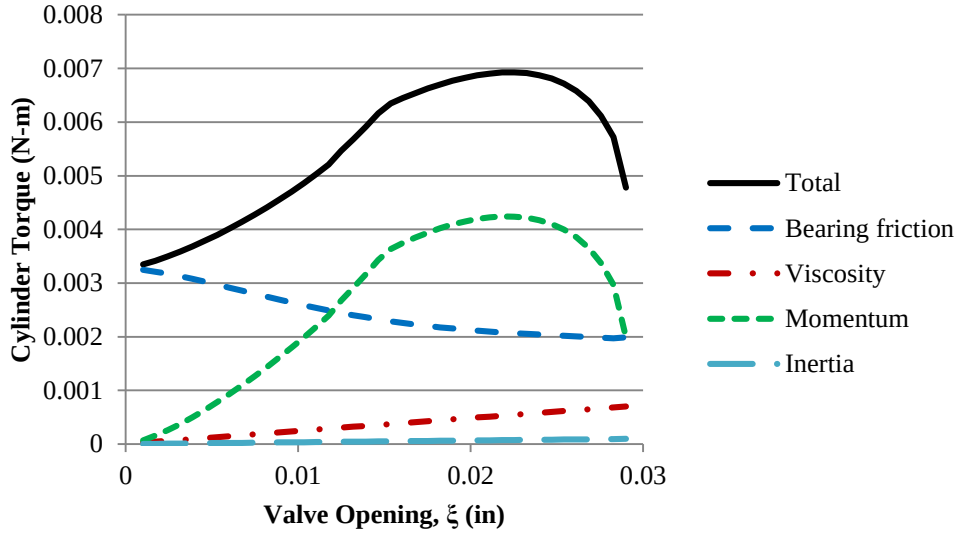

Figure 3-8. Cylinder torque load components at a given valve opening.

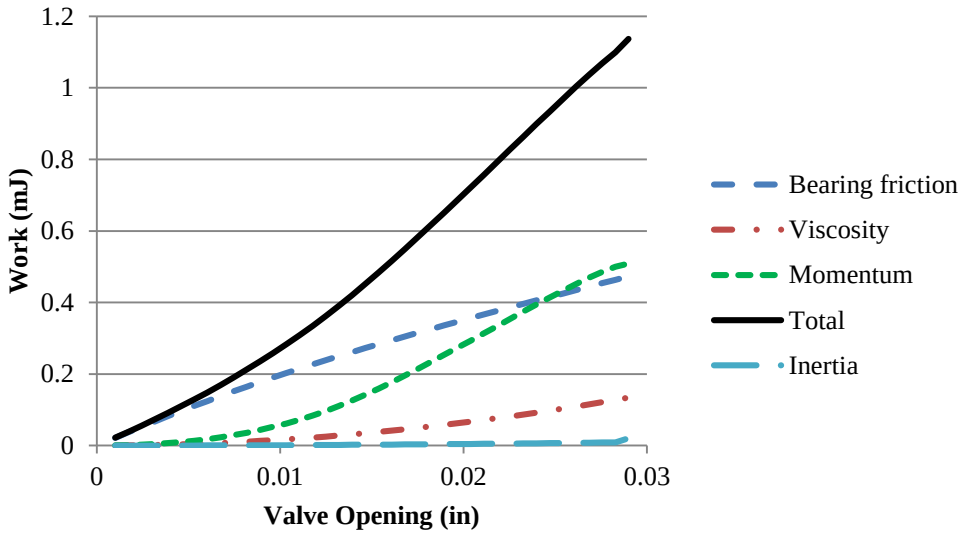

Figure 3-9. Components of the work to rotate cylinder to a given valve position.

It should be observed that the primary torque load source is due to bearing friction, which suggests that altering the design to better balance the pressure loads on the cylinder is highly recommended.

3.6 Spool Valve

In order to establish a basis for comparison, an examination of the actuation power required to operate a linear spool valve is required. In a linear spool valve, a flanged cylinder is actuated axially along a cylindrical housing that contains multiple ports for flow control. For this comparison, the geometry of the Moog Series 24 servo valves is used, as it represents the latest state-of-the-art in miniature servo valve technology and is currently used in the Merlin initiative. An illustration of the spool valve geometry is shown below in Figure 3-10. Another reason is that one of the key design parameters required for fluid flow analysis, the radial clearance between the spool and the housing, was made available by the manufacturer and thus allows a more accurate estimation of the flow forces at work.

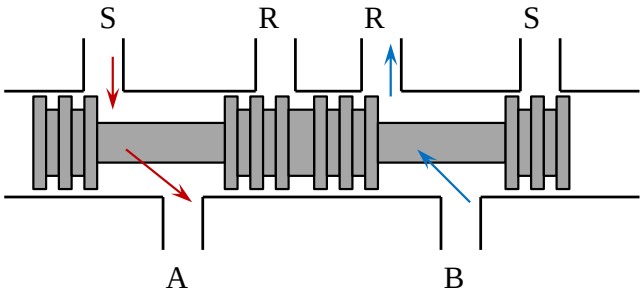

Figure 3-10. Illustration of the Series 24 servo valve spool. Pressure supply, are denoted as *S* and *R*, respectively. Ports *A* and *B* denoted accordingly.

3.6.1 Valve Geometry

A representation of the key geometric parameters of the spool valve used in the analysis is shown below in Figure 3-11. These key terms include the spool head diameter, d_H, the shaft diameter, d_s, the housing bore diameter, d_b, the flow port width, d_p, the radial clearance between the spool and the housing, c_r, and the length between spool lands, L, and the width of the orifice opening, ξ. The fluid pressures at each port are identified with the port designation subscript. With the exception of the radial clearance, which was provided directly from the manufacturer, all other dimensions were pulled from a CAD model of the spool valve architecture provided by Moog. The valve is assumed to be symmetric such that the orifice width for the supply and return ports are equal at all spool placements.

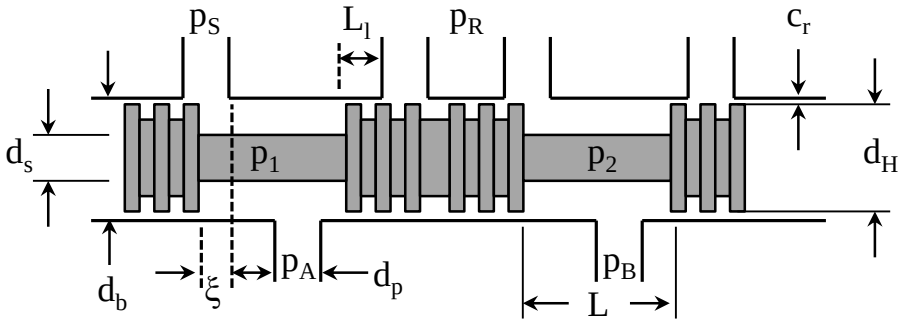

Figure 3-11. Spool valve geometric parameters.

3.6.2 Spool Valve Force Balance

As the goal of the analysis is to determine the force and power required to actuate the spool, the forces of interest are those that act in the axial direction. The use of the Reynolds Transport Theorem in

Equation (3.1) still describes the momentum force on the valve spool, which can be similarly separated into steady and transient flow forces. There are six flows of interest, shown in Figure 3-12, within the spool control volume: flow into and out of the spool through the supply and return ports, flow into and out of the spool through ports A and B, and leakage across the spool head. The leakage flow consists of two components, one from the closed supply port into the return section of the spool, and flow from the pressure supply section of the spool to the closed return port. For a partially open valve, the flows from supply and to return, Q_S and Q_R, respectively, are jets at an angle to the axis of the spool, θ.

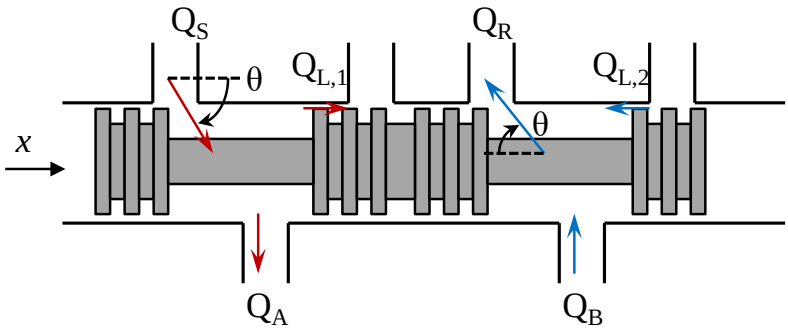

Figure 3-12. Spool component flows.

The axial momentum force on the spool can be written as

$$F_x = \frac{\rho}{A_o}\cos\theta\left(Q_S^2 + Q_R^2\right) + \frac{\rho}{A_L}\left(Q_{L,1}^2 + Q_{L,2}^2\right) + \rho L\frac{\partial}{\partial t}\left(Q_S - Q_R\right) \tag{3.47}$$

where A_o and A_L are the orifice and leakage flow areas. Note that the steady momentum force due to the jet will always act to close the valve.[1] Flow through ports A and B are purely radial with no jet formation, as by design the spool lands do not obscure the two ports, thus they do not contribute to axial load on the spool. Thus the steady and transient flow forces can be defined.

$$F_s = \frac{\rho}{A_o}\cos\theta\left(Q_S^2 + Q_R^2\right) + \frac{\rho}{A_L}\left(Q_{L,1}^2 + Q_{L,2}^2\right) \tag{3.48}$$

$$F_t = \rho L\frac{\partial}{\partial t}\left(Q_S - Q_R\right) \tag{3.49}$$

The jet angle, θ, can be determined from Equation (3.6). It is important to note that for the geometry of the Series 24 valve, the momentum forces from the jets at the supply and return ports are in the same direction and thus additive. Conceptually, this is due to the spool first turning the supply jet flow to the left, followed by turning the flow from port B to the left again by the jet into the return port. The reaction force from the flow thus imparts a force on the spool to the right, or positive x direction. The orifice area for a square port and the leakage flow area are given by

$$A_o = d_p\xi \tag{3.50}$$

$$A_L = \pi c_r d_H \tag{3.51}$$

The flow rate through the supply and return jets can be calculated as an idealized orifice flow using a discharge coefficient, C_d,

$$Q_S = C_d A_o \sqrt{\frac{1}{1-\left(d_{o,h}/d_p\right)^4}} \sqrt{\frac{2\left(p_S - p_1\right)}{\rho}} \tag{3.52}$$

$$Q_R = C_d A_o \sqrt{\frac{1}{1-\left(d_{o,h}/d_p\right)^4}} \sqrt{\frac{2\left(p_2 - p_R\right)}{\rho}} \tag{3.53}$$

In order to readily calculate the conditions within the valve analytically, the supply flow rate is assumed as an operating condition, which allows for solving for the pressures in the spool using the equations below.

$$p_1 = p_S - \frac{\rho Q_S^2}{2C_d^2 A_o^2}\left(1-\left(\frac{d_{o,h}}{d_s}\right)^4\right) \tag{3.54}$$

$$p_2 = p_R + \frac{\rho Q_R^2}{2C_d^2 A_o^2}\left(1-\left(\frac{d_{o,h}}{d_s}\right)^4\right) \tag{3.55}$$

The leakage across the spool lands are calculated as Couette flow between the housing inner diameter and the motion of the spool lands,

$$Q_{L,1} = \frac{\pi r_H c_r^3\left(p_1 - p_R\right)}{6\mu L_l} + \pi r_H u_H c_r \tag{3.56}$$

$$Q_{L,2} = -\frac{\pi r_H c_r^3\left(p_S - p_2\right)}{6\mu L_l} + \pi r_H u_H c_r \tag{3.57}$$

where L_l is the length of the leakage pathway, set by the length of the land separating the return or supply port from the valve chambers, and u_H is the velocity of the spool. The leakage is defined such that positive leakage is out of the control volume, and negative leakage is into the control volume. The leakage pathway length is modeled in terms of the orifice opening width and the spool overlap, L_{OL}.

$$L_l = \xi + 2L_{OL} \tag{3.58}$$

The factor of two for the spool represents the overlap at the leakage point plus the additional distance the spool must move to overcome the overlap at the jet orifice, as overlaps are assumed to be identical at each port in the null position.

The simultaneous use of Equations (3.48) through (3.58) in combination with a defined supply flow rate, as well as supply and return pressures, will enable calculation of the steady and transient

momentum loading on the spool. The other primary source of loading on the spool is viscous shear on the spool, which can be divided into friction at the spool head, $F_{f,H}$, and friction along the shaft of the spool, $F_{f,s}$,

$$F_{f,H} = 2\pi r_H \mu \left(\frac{u_H}{c_r} L_H + \frac{c_r \Delta p}{2\mu L_l} \right) \tag{3.59}$$

$$F_{f,s} = \pi (\Delta p_1 - \Delta p_2) \left[r_s^2 - \frac{r_b^2 - r_s^2}{2\ln(r_b / r_s)} \right] \tag{3.60}$$

where L_H is the total length of all the spool heads, and Δp_1 and Δp_2 are the pressure drops across the individual chambers of the valve. Due to the very small radial clearance between the spool head and the housing, the first term of Equation (3.59) dominates such that the friction along the shaft is negligible.

The total axial force on the spool can then be calculated as the sum of the steady, transient, and frictional forces.

$$F_{spool} = F_s + F_t + F_{f,H} \tag{3.61}$$

The power expended to actuate the spool can then be calculated in terms of the spool force and the spool velocity.

$$P_{valve} = u_H F_{spool} \tag{3.62}$$

3.6.3 Case Study

To compare the rotary valve performance with an example of the state-of-the-art for commercially available spool valves, the geometry of the Moog Series 24 servo valve spool is used for the case study. The the operating conditions for the calculations are given below in Table 3. The geometric parameters, with the exception of the radial clearance which was supplied by the manufacturer, have been inferred from a CAD model supplied by Moog, but have been left out to protect Moog proprietary information

Table 3. Operating conditions of spool valve case study

ρ_c	2700 kg/m^3
ρ_f	850 kg/ m^3
μ_f	0.0187 kg/m-s
C_d	0.9
Q_S	0.5 gpm
p_S	2900 psi
p_R	14.5 psi
t_{res}	3 ms

There are two primary axial loads on the spool: the steady momentum force and the friction between the spool head and the spool housing, shown in Figure 3-13. The transient momentum force was found to be three orders of magnitude less than the steady momentum force, and the shear force on the shaft was found to be negligible. As in the case of the rotary valve, the dominant load changes as the valve opens. For small valve openings, the steady momentum force from the axial component of the fluid jets at the ports dominate. As the valve opens, the jet angle increases and the axial component of the force decreases. At the same time, as the desired valve opening increases, the velocity of the spool must increase in order to achieve the desired displacement in the specified response time; this increases the frictional force on the spool. It should be noted that there is a point of non-differentiability of the steady momentum force term. This is the point of transition from Equation (3.6) to Equation (3.7) is an artifact of this arbitrary shift in jet angle definition.

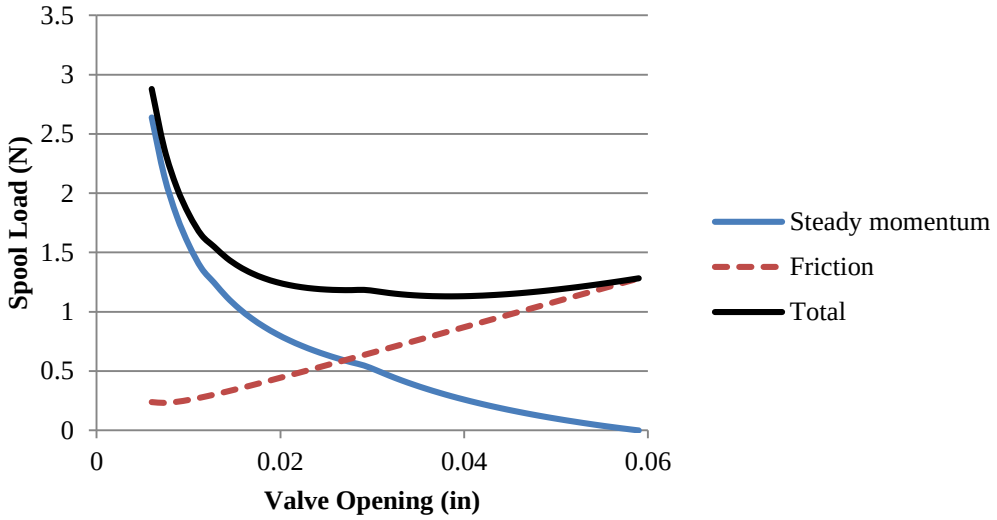

Figure 3-13. Axial forces on the spool as a function of valve opening.

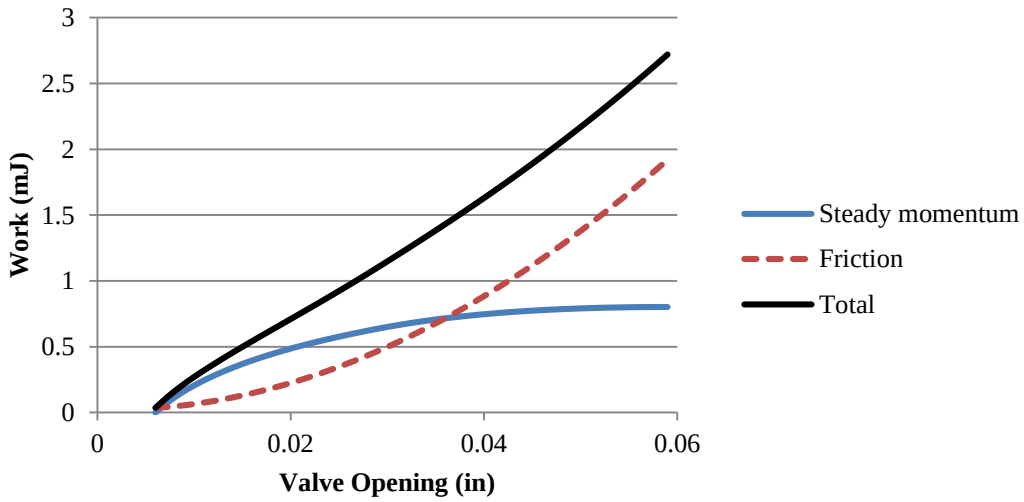

Figure 3-14. Work required to actuate spool to a given valve position from null position.

3.7 Comparison

To best compare the rotary and spool valve configurations, the net work required to actuate the valve as a function of a normalized valve opening (ξ/d_p) is compared for both valves. The plot of the two work curves, shown in Figure 3-15, illustrates the greater amount of work required to actuate the spool valve compared to the rotary valve.

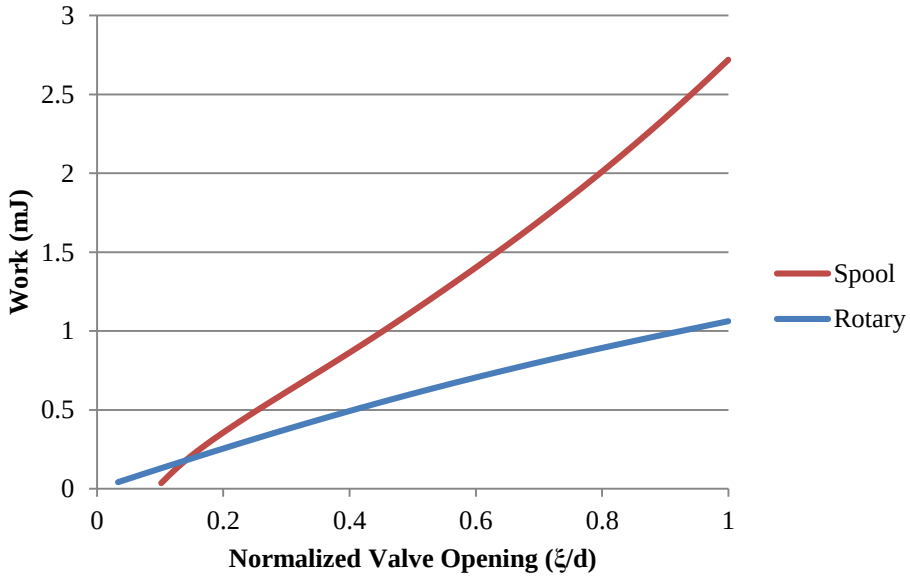

Figure 3-15. Comparison of valve actuation work as a function of normalized valve position.

4.0 Valve Development Progress

The process for developing the valve was to:

1. Establish an analytical model for spool loading as a function of spool position and valve operating conditions.
2. Develop fabrication methods for the valve spool and housing.
3. Create an instrumented spool load testbed to validate the analytical model to provide a baseline set of design criteria for the valve actuation.
4. Identify what novel technology can be leveraged for high-precision actuation of the spool to provide sufficient flow regulation.
5. Integrate the above elements into a valve prototype.

The first step of this was addressed in Section 3.0, while this section covers the progress achieved with the remainder of the process. Each of these steps addressed a key challenge with the rotary valve concept. The first to be discussed here is the development of fabrication methods to produce high-precision, small-scale components that could provide the internal passages required to route the flow such that the hydrodynamic forces could be balanced to reduce overall spool torque, while limiting internal flow leakage and frictional losses. The next challenge to be discussed is the validation of the analytical spool load model against empirical data collected on a spool load testbed. This would provide a baseline for the required torque output for the valve actuator and refine selection of commercial actuators, as well as present an opportunity for testing the valve architecture. With this completed, selection of the valve actuator could be conducted, along with a means of precise control of the spool position. With the completion of these steps, the lessons learned could be leveraged to design a valve prototype for further testing and optimization.

4.1 Fabrication Methodology

Work on component fabrication was conducted with assistance from Dr. Charles Rohde and Robert Leary in Code 7165 and made use of their Concept M2 Cusing laser system, which could additively manufacture parts in SS316. There were two primary features desired for the components: precise internal passages, and a honeycomb lattice structure for mass reduction. The internal passages were critical for routing fluid through the valve spool and housing such that flow into and out of the spool would provide antagonistic torque loading, thereby reducing the net torque load on the spool. The honeycomb lattice structure was to ensure minimal valve mass, as the targeted application (a hydraulic quadruped) was still highly mass-constrained. Figure 4-1 shows a CAD rendering of the desired traits demonstrated in the spool load testbed.

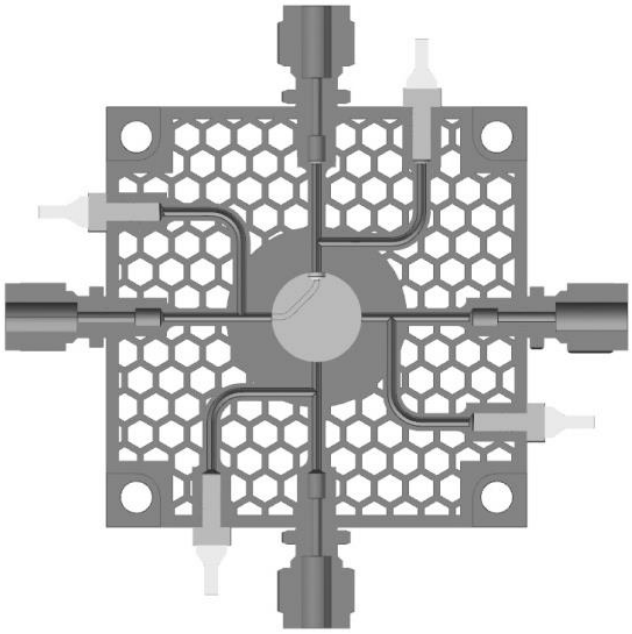

Figure 4-1. CAD rendering of a top-down cross section of the spool load testbed. The image displays the two key traits desired: internal passages to route fluid and a honeycomb lattice to support the primary features.

4.1.1 Initial Fabrication Samples

An initial run of test components was printed and then sectioned using wire electrical discharge machining (EDM). The sections were placed as to bisect the cross section of the internal passages, similar to the CAD representation in Figure 4-1. The cut sections were then examined using a Keyence VHX digital microscope to capture the precision of the passage cross sectional profile and surface roughness. Figure 4-2 presents two example microscope images of a sectioned test part, particularly of the wide inlet port of the spool. The images revealed that while the bottom portion of the port was of the desired shape, the top portion had noticeable irregularities. When quantified along a specified line segment, the top profile was distinctly more irregular compared to the bottom profile, shown in Figure 4-3.

Figure 4-2. Microscope imaging of a sectioned test spool: the top half with the honeycomb lattice and internal passage (*left*), and a close up of the bottom half of the inlet port.

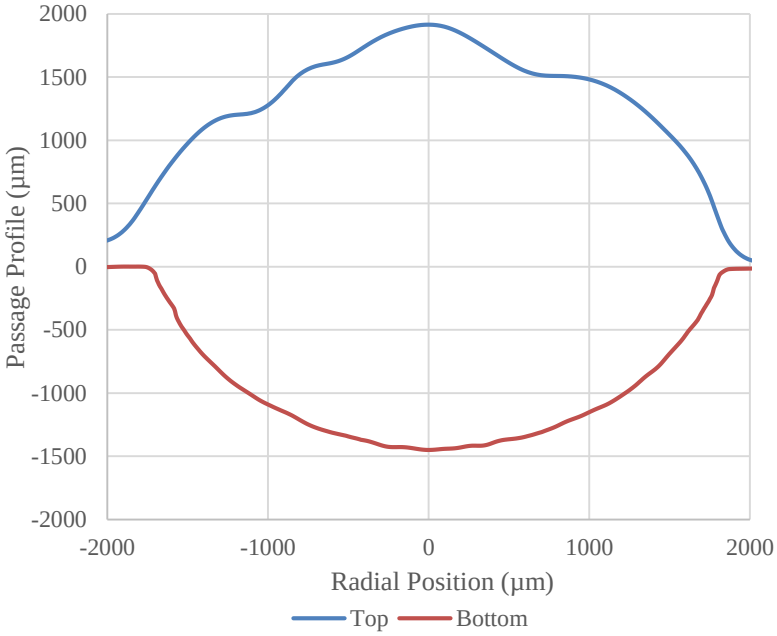

Figure 4-3. Measured passage inlet port profile height relative to the section cut.

This relative increase in profile irregularity of the top compared to the bottom was also present in the internal passageway beyond the inlet port. Figure 4-4 demonstrates how even in the smaller passage, the top half was much more irregular, while the bottom half was relatively smooth and consistent. A comparison of axial profiles along the top and bottom halves of the passage confirmed a greatly increased roughness along the top half compared to the bottom half, shown in Figure 4-5.

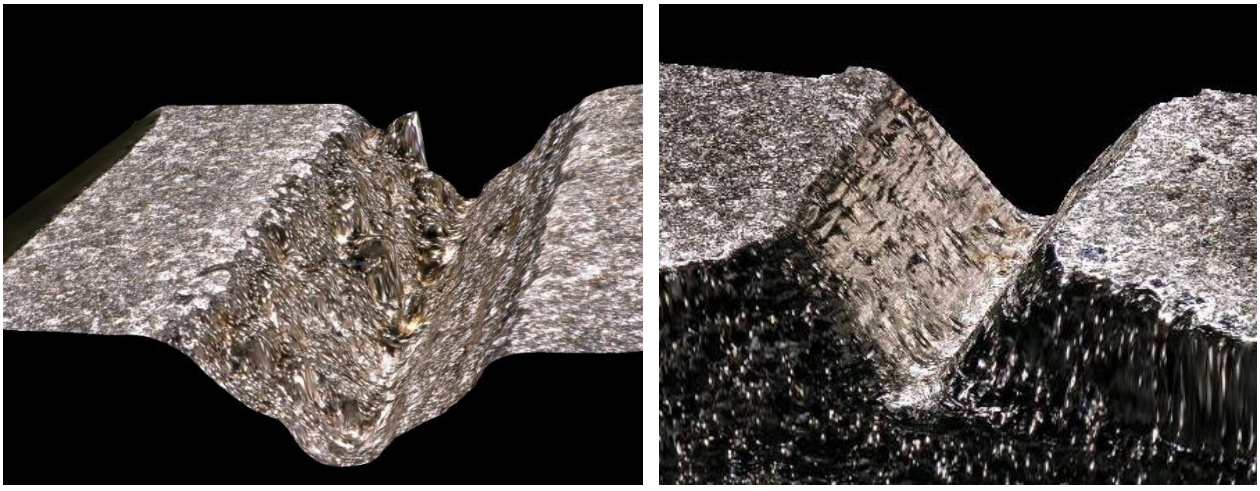

Figure 4-4. 3D microscope rendering of the top (*left*) and bottom (*right*) halves of a section of the internal passage within the test spool. The top half contained a greater degree of irregularity compared to the bottom half.

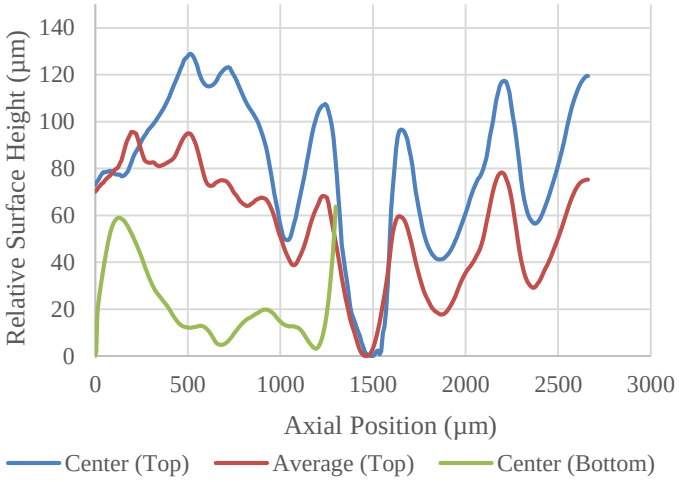

Figure 4-5. Comparison of axial profiles along the interior spool passage. Blue line denotes the centerline profile of the top half, the red line is an average of multiple axial profiles along the top, and the green line is the center profile of the bottom half.

This issue also extended to the interior passages within the valve housing, as shown in Figure 4-6. It should be noted that the section cut for the valve housing was not as accurately placed to bisect the passage, and thus the cut removed more material from the top half than the bottom half, making the top half appear smaller. The measured profile of the passage confirms that the top half is more irregular than the bottom half, as shown in Figure 4-7. A comparison of two different profiles along the length of the passage, shown in Figure 4-8, reveals that the irregularities result in a variable passage cross-sectional area along the length of the passage.

Figure 4-6. Comparison of the top (*left*) and bottom (*right*) halves of the internal passage in the valve housing. The section cut did not cleanly bisect the passage, placing more of the cut in the top half, and thus reducing its apparent width.

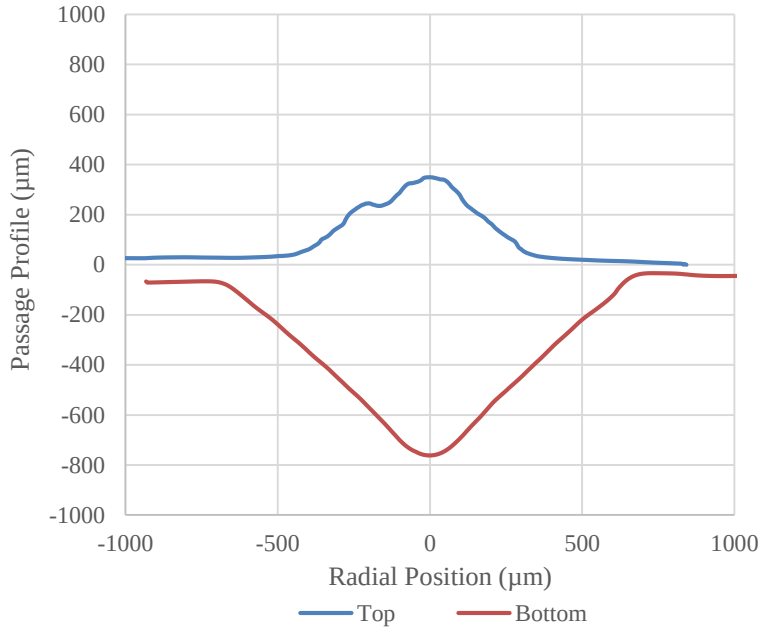

Figure 4-7. Measured valve housing internal passage profile height relative to the section cut.

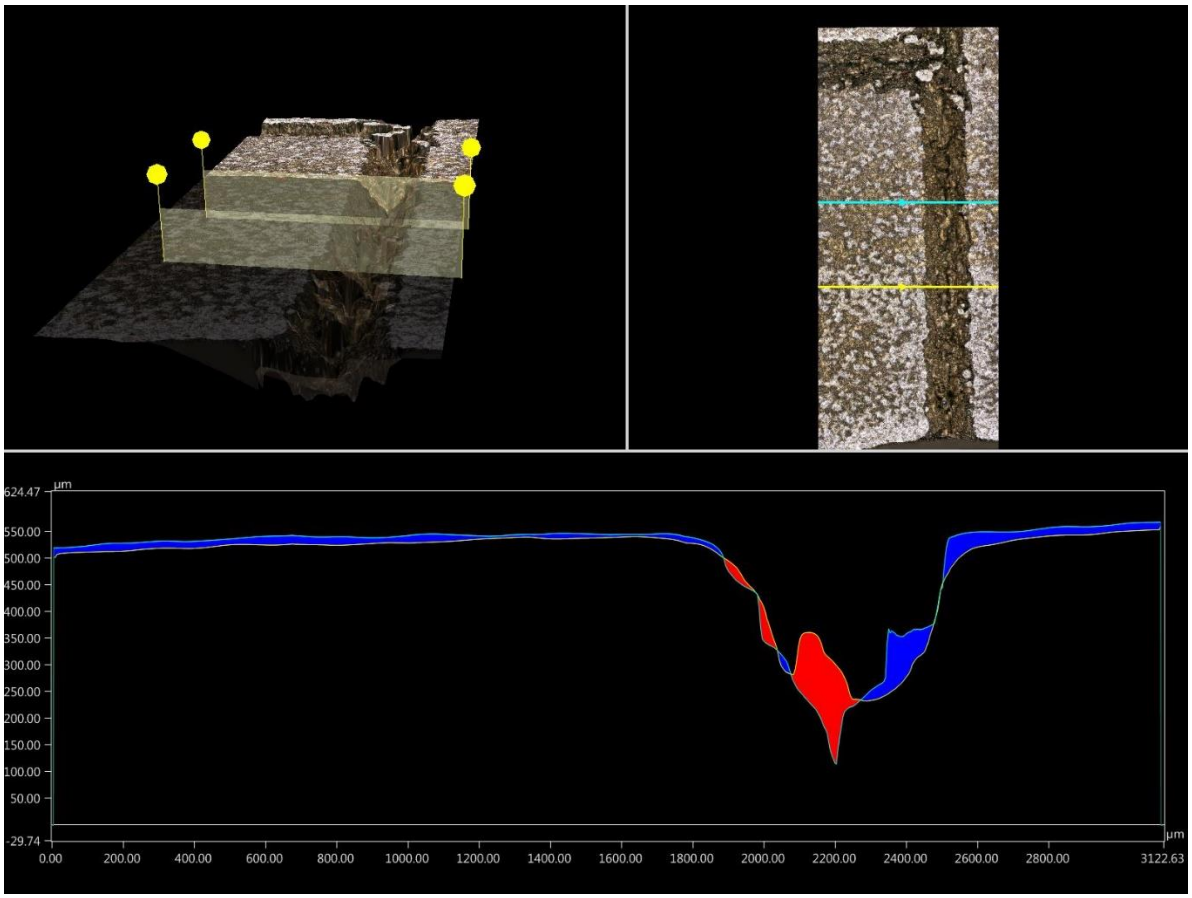

Figure 4-8. Profile variation in the top half of the valve housing passage. 3D (*top left*) and 2D (*top right*) representations of the placement of the two profiles, and superposition of the two profiles (*bottom*).

The combination of irregularity and the unpredictability of the irregularity within the internal passages is problematic for two reasons. The first reason is that such irregularities facilitate the transition of the flow into turbulence and could potentially create recirculation within the passage, which could greatly complicate modeling. The second reason is that hydrodynamic force on the spool is a function of the jet angle and the area of the orifice created by the opening of the spool passage. If the cross-section of the internal passage is irregular and variable, then the angle of the jet may not match what is predicted by Equation (3.6), and the force imparted on the spool could be highly variable between multiple spools despite having nominally the same design. It was theorized that the irregularities were due to either the weld melt dripping during fabrication, or potentially warping of the structure due to insufficient support of the arch as it is built up. Eliminating this phenomenon was outside the scope of the project, so therefore it was necessary to determine a passage cross section that could be readily fabricated using existing equipment and methods while still providing a clean, repeatable, and consistent cross section upon fabrication.

4.1.2 Internal Passage Cross Section Study

In order to ascertain the optimal cross section of the internal passage that could be printed, a comparative study was conducted with nine candidate shapes, each of roughly equivalent area. A sample part was designed where each shape was centered along a line to enable sectioning with wire EDM to compare the resulting profile of the top half of the passage. Since the irregularities were a result of insufficient support of the apex of the passage, each of the nine candidate shapes completed in a point. Table 4 presents a summary of the shapes tested, with the test part displayed in Figure 4-9.

Table 4. Summary of Candidate Shapes

Index Number	Shape	Apex Angle (°)
1	Tear drop	60.0
2	Tear drop	38.9
3	Concave tear drop	49.2
4	Diamond	59.8
5	Equilateral triangle	60.0
6	Isosceles triangle	39.7
7	Convex tear drop	53.1
8	Tipped convex tear drop	40.0
9	House	53.1

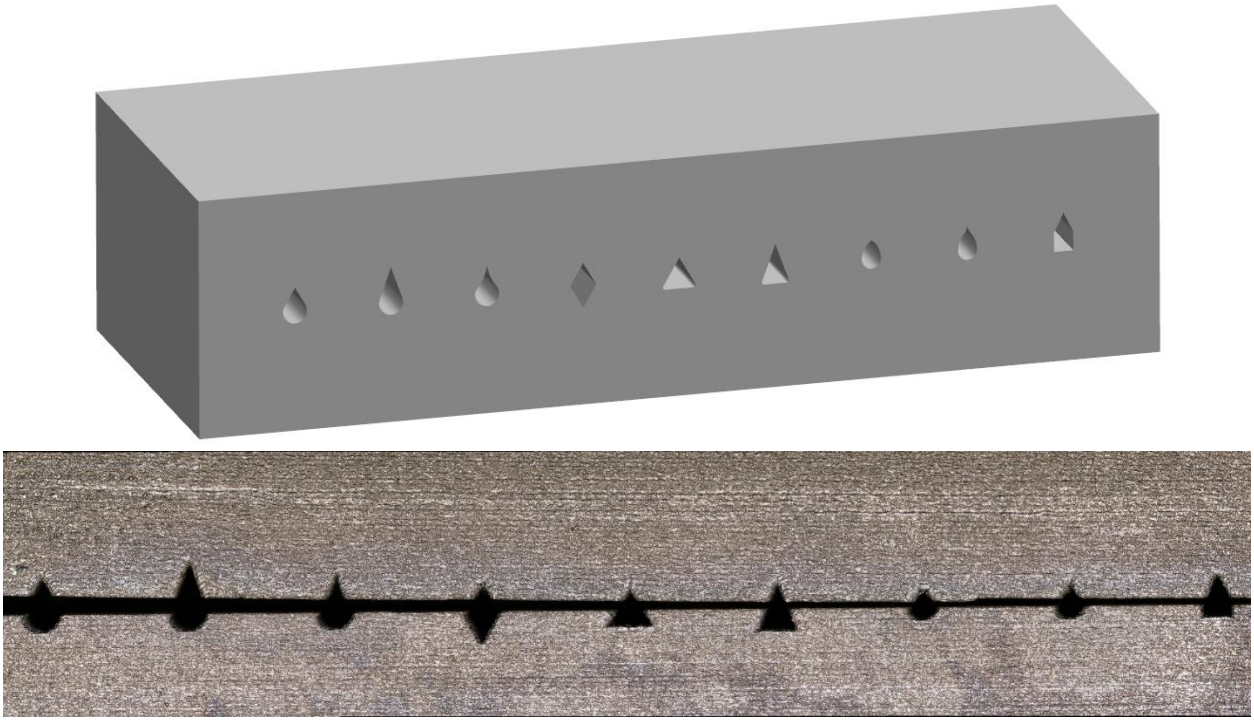

Figure 4-9. Sample part with the nine candidate shapes; (*top*) CAD rendering of the part, and (*bottom*) microscope image of the two halves after sectioning with wire EDM. The shapes are numbered 1-9 from left to right, corresponding to the shapes listed in Table 4.

After sectioning, the two halves of the test part were inspected using a digital microscope to capture the transverse profile of each resulting passage. The shapes were then qualitatively graded on the consistency of the transverse and axial profiles. A subset of the transverse profiles is shown in Figure 4-10.

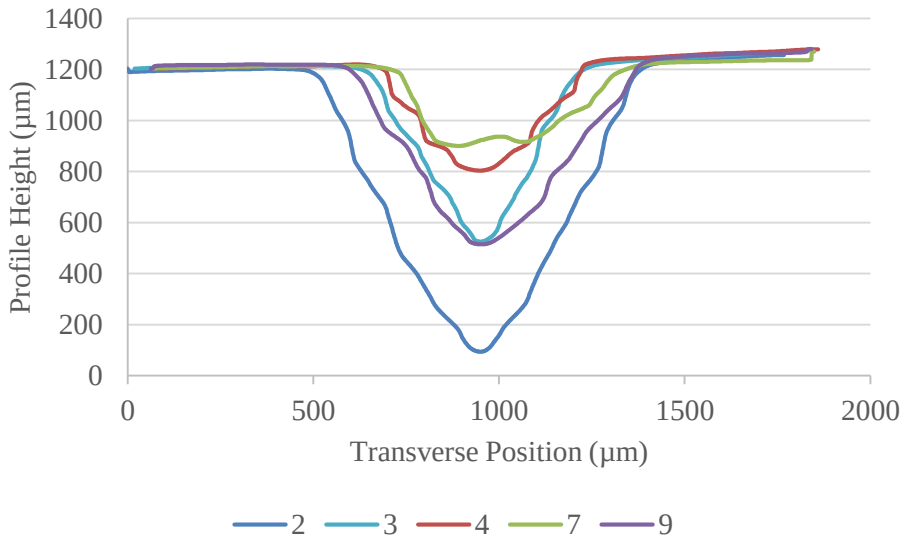

Figure 4-10. Comparison of a subset of the top halves of the resulting passages of the sample part.

Several takeaways from this study include:

- Concave or convex shapes at this size scale (approximately 0.04”-0.07” wide) did not survive fabrication, instead losing definition to the point of appearing like misshapen triangles
- Curvature on the bottom portion of the passage was obtainable, but less uniform compared to flat surfaces
- Variation of the apex had negligible impact on the rest of the top portion of the passage (i.e. the addition of a narrow tip to the top of the tear drop in shape #8 did not provide any additional stability during fabrication compared to shape #7, despite being otherwise identical
- In general, higher shape stability is found with decreasing apex angle

The two leading candidates were shapes 2 and 9. In order to further select between these two shapes, a comparison was made of the open orifice area as a function of spool position. A desired trait of a servo valve is that the behavior of the valve is relatively linear with spool position. Figure 4-11 shows that shape #9 had a more linear behavior, particularly at a low degree of spool openness. Therefore, the house shape was selected as the shape for the internal passages to maximize the consistency of the passage cross sectional area.

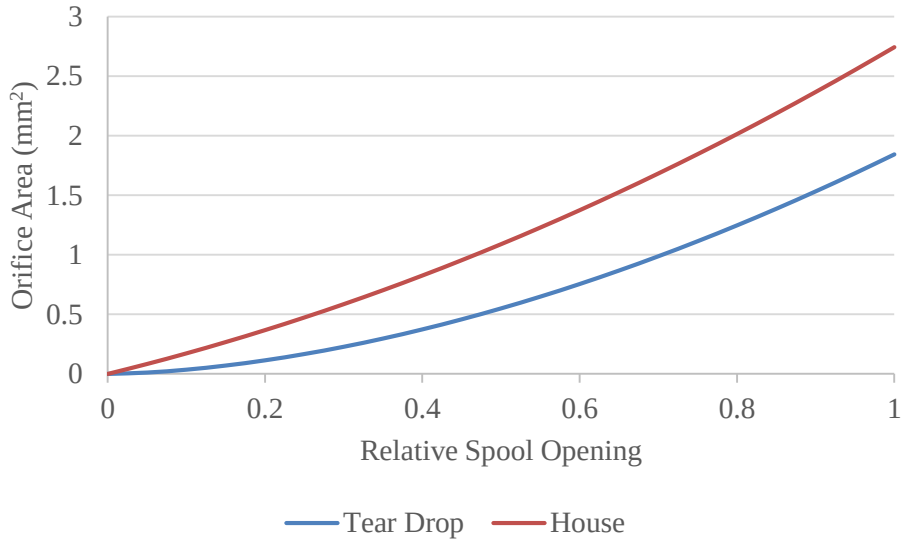

Figure 4-11. Comparison of the open orifice area as a function of the relative spool opening.

4.2 Spool Load Study

Once the fabrication methodology was established, a prototype testbed could be built where the hydrodynamic loading on the spool could be measured and used to validate the analytical model. To facilitate torque measurement and simplify design and machining constraints, an oversized spool geometry was utilized. The spool is then housed in an oversized, simplified housing with internal fluid routing with pressure taps for each port. Multiple spool designs could then be used to test the torque loading for different internal passage designs. The combination of a motor, torque transducer, and rotary encoder provided the means of setting spool position while measuring the torque required to maintain it. Figure 4-12 shows a CAD representation of the spool load testbed.

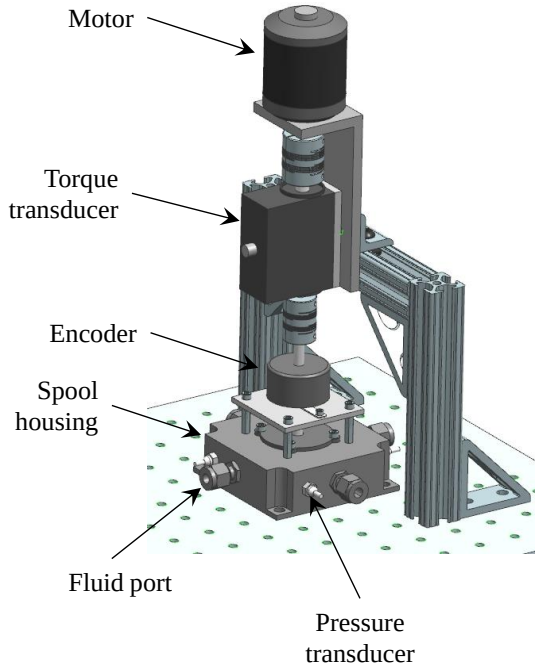

Figure 4-12. CAD rendering of the spool load testbed.

The testbed was designed to use a drive shaft to connect the spool to the torque transducer while passing through a rotary encoder. The drive shaft is sealed using a labyrinthine seal that cuts into a PTFE washer to ensure a low-friction seal that can minimize leakage for fluid pressures up to 500 psi. The spool rests on a thrust bearing placed at the bottom of the spool receptacle in the housing to reduce friction during actuation of the spool. The thrust bearing can also be shimmed to ensure precise alignment of the ports within the spool to the ports in the housing.

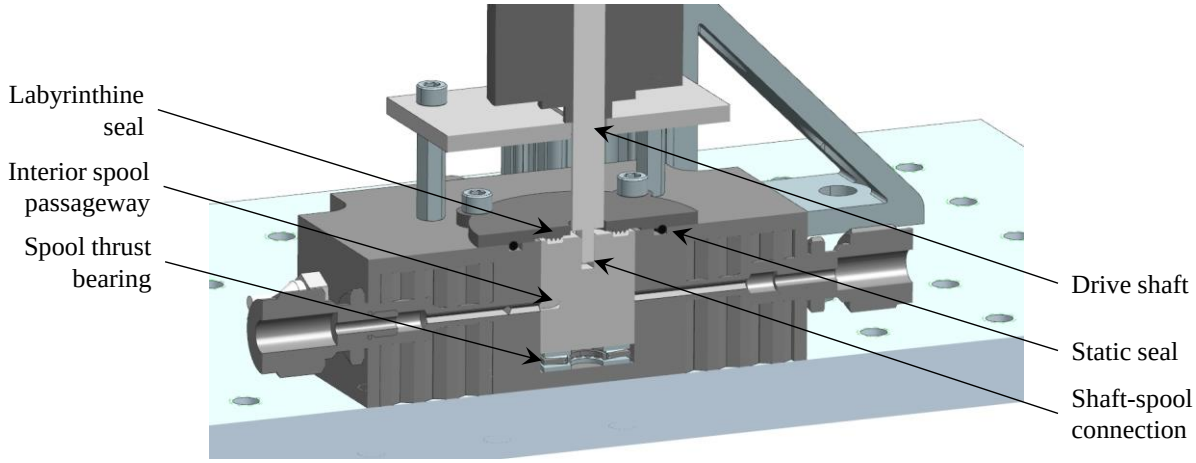

Figure 4-13. CAD rendering of a cross section of the spool load testbed.

Initial testing would involve three spool designs:

- One-sided, single orifice
- One-sided, double orifice

- One-sided, antagonistic double orifice

One-sided refers to the spool containing only a single internal passage that connects two fluid ports (e.g. supply port to port A). This acts to limit the number of active jets to two and facilitates isolating the impact of spool position on the resulting torque load. Single and double orifice refer to whether the spool passage has one or two narrow ports that do not extend beyond the nominal passage cross section. The single orifice spool has one port expanded into a larger circular cross section, an example of which is shown in Figure 4-2. The antagonistic spool is designed such that the angular displacement of the ports on the spool is slightly smaller than the angular displacement of the corresponding ports on the housing. This results in neither port being fully open at the same time. Since the torque load on the spool induced by the jet flow through an orifice acts to close the orifice, this should place the torque load from both spools in opposition, thus reducing the net torque on the spool.

4.3 Valve Actuation and Control

The spool load testbed was originally designed to utilize the brushless DC motors already on-hand from the MeRLIn program. Brushless motors are compact and efficient with an existing control infrastructure through commutation control circuitry. Spool position could then be set using a PID control loop on the output of the rotary encoder. However, a critical limitation with brushless motors for this application is that torque is produced through the interaction between current-carrying coils and magnetic poles. The number of coils and poles dictates the number of stable motor positions, which means that when attempting to perform small angular displacements the motor will either overshoot to the next stable position or oscillate around an unstable position. Figure 4-14 shows a plot of set and actual spool position over time, which generally resulting in approximately 2° of error. Given the small size of the ports involved, this was considered insufficient precision for the application. Investigation into an alternative actuation source resulted in the adoption of an ultrasonic motor as the prime mover.

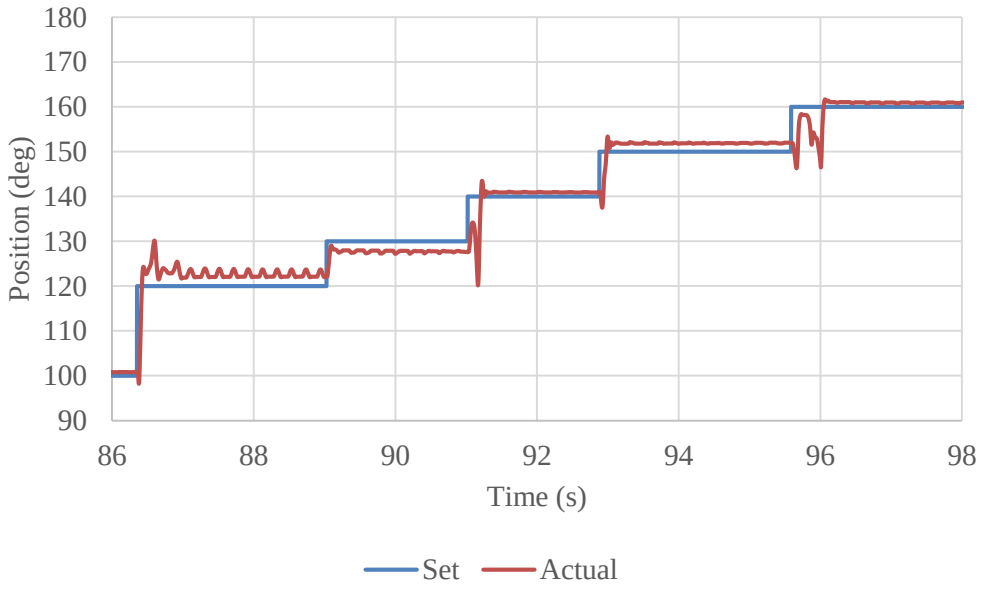

Figure 4-14. Set and actual spool position using a PID control loop on a brushless DC motor.

4.4 Interruption due to COVID-19

Progress into the spool load testbed was halted in early 2020 due to the outbreak of COVID-19 limiting laboratory access. The ARTHuR project shared laboratory space with several other projects, and due to ongoing activity the room's occupancy limit was reached. Effort was shifted to the modeling and control element of the program, as it could be continued remotely.

5.0 Hydraulic System Model Derivation

One research effort of the ARTHuR program is to determine how the locomotion algorithm can be modified to enable predictive control of the hydraulic powertrain to better regulate system flow. As part of this effort, a simulation framework is required to enable testing of algorithm modifications. The model can be broken into two sections: a hydraulic model than captures the powertrain and valve-actuator dynamics, and a kinematic model that captures the behavior of the quadruped in response to the actuators. The kinematic modeling is conducted by an external software package, MuJoCo Advanced Physics Simulation. Simulation of the hydraulic system was developed internally using a combination of analytical and empirical formulations.

The model is based on the Butch quadruped architecture developed under the MeRLIn program. A hypothetical hydraulic power unit (HPU) is assumed based on user-defined operational parameters, such as nominal system flowrate. The HPU supplies fluid to a manifold that houses 12 servo valves that in turn control fluid flow to 12 linear actuators. The pressure in the manifold is regulated by a spring-loaded relief valve that returns excess fluid to the HPU reservoir. A schematic of the hydraulic model is shown below in Figure 5-1.

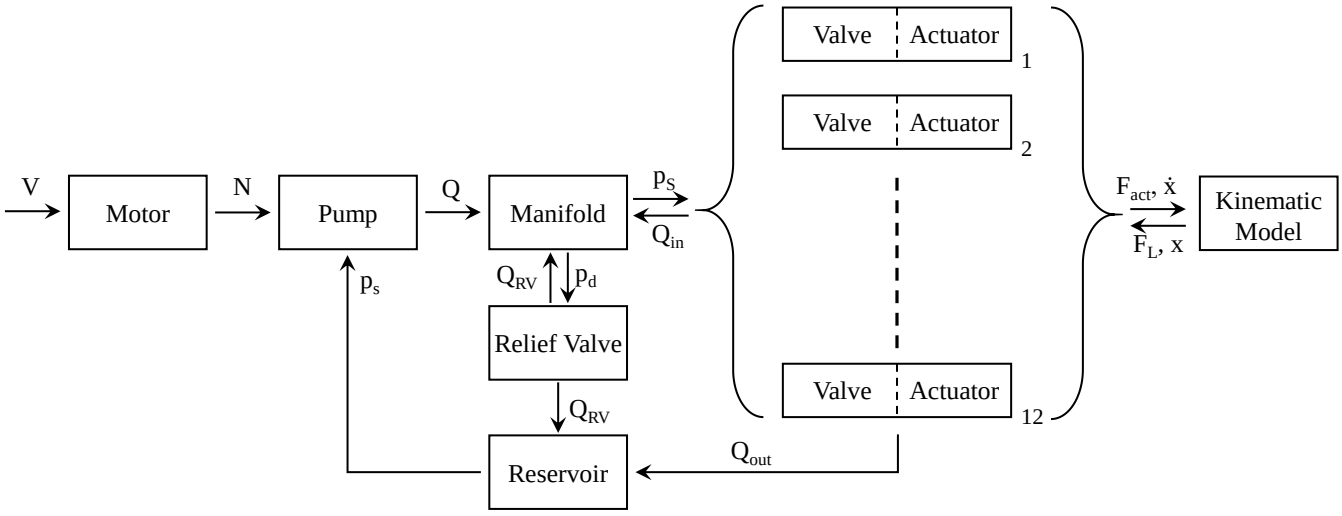

Figure 5-1. Overall schematic of the hydraulic model.

5.1 Motor

The motor is assumed to be a brushless direct current (BLDC) motor similar to what was used in the MeRLIn program.[3] The line-to-line voltage, *V*, applied to the motor is spent on two terms,

$$V = I_L R_{LL} + K_e N \tag{5.1}$$

where I_L is the line current, R_{LL} is the line-to-line resistance, K_e is the motor back-emf constant, and N is the motor speed in rpm. The line current can be replaced using the definition of the motor torque constant, K_T,

$$V = \frac{\tau_m}{K_T} R_{LL} + K_e N \tag{5.2}$$

where τ_m is the output motor torque. Rewriting Equation (5.2) in terms of the motor torque yields

$$\tau_m = \frac{K_T}{R_{LL}} (V - K_e N) \tag{5.3}$$

It is worth remembering that the torque and emf constants are related by the equation below, where K_e is in V/rpm, and K_T is in N-m/A.

$$K_e = \frac{2\pi}{60} K_T \sqrt{2/3} \tag{5.4}$$

The total motor torque is the sum of the inertial torque, the frictional torque, and the load torque, τ_L,

$$\tau_m = J_{tot}\alpha + b\omega + \tau_L \tag{5.5}$$

where α is the angular acceleration, J_{tot} is the total moment of inertia, b is the effective damping of the system, and ω is the angular velocity. Note that the motor torque is limited based on the maximum current of the motor multiplied by the torque constant. From empirical data, the torque load of the pump can be approximated as a linear dependency on the pressure rise across the pump, Δp.

$$\tau_L = c_L \Delta p \tag{5.6}$$

The load coefficient, c_L, can be calculated with reasonable accuracy (within 4%) from the pump gear geometry,

$$c_L = r_p (a + b) w \tag{5.7}$$

where r_p is the pitch radius, a is the addendum, b is the dedendum, and w is the width of the gear.

Recalling that angular velocity and angular acceleration can be defined in terms of N,

$$\omega = N \frac{2\pi}{60} \tag{5.8}$$

$$\alpha = \frac{dN}{dt} \frac{2\pi}{60} \tag{5.9}$$

Leveraging the above two relations, Equation (5.5) can be rewritten as a differential equation of the shaft speed.

$$\frac{dN}{dt} = \frac{1}{J_{tot}}\left(\frac{60}{2\pi}\tau_m - bN - \frac{60}{2\pi}\tau_L\right) \tag{5.10}$$

Substituting Equations (5.3) and (5.6) into Equation (5.10) yields the characteristic equation of the motor model as a function of motor voltage, motor speed, and pump pressure differential.

$$\frac{dN}{dt} = \frac{60}{2\pi J_{tot}}\left[\frac{K_T}{R_{LL}}V - \left(\frac{K_T K_e}{R_{LL}} + \frac{2\pi b}{60}\right)N - c_L\Delta p\right] \tag{5.11}$$

The total moment of inertia is the sum of the motor moment of inertia, J_{motor}, and the pump moment of inertia, J_{pump}. The motor moment of inertia can be found empirically from motor acceleration under no-load conditions.

5.2 Gear Pump

The gear pump model is based on analytical and empirical work done for the MeRLIn program. The output flow rate of the pump is dependent on the shaft speed, N, pump displacement, D, and the pump volumetric efficiency, η_v.

$$Q = \frac{\eta_v N D}{60} \tag{5.12}$$

The displacement is defined as ideal volume output per revolution of the pump, and the shaft speed is given in rpm. The volumetric efficiency can be modeled as a function of the shaft speed and the pump pressure differential, Δp.

$$\eta_v = 1 - \frac{60\Delta p}{N D R_G} - \frac{1}{D\mathbb{R}_G} \tag{5.13}$$

In the above equation, R_G and $\mathbb{R}_G$ are constants that define the pump efficiency across a range of operating conditions. These constants cannot readily be derived, but instead are most easily determined empirically for a given pump. However, since the constants are related to the internal tolerancing between pump components, within a reasonable range of pump sizes from those tested under MeRLIn we can assume the values found in previous empirical studies.[4]

Substituting Equation (5.13) into (5.12) yields the characteristic equation for modeling the pump in terms of the shaft speed and the pump pressure differential.

$$Q = \frac{N}{60}\left(D - \frac{1}{\mathbb{R}_G}\right) - \frac{\Delta p}{R_G} \tag{5.14}$$

The remaining unknown is how to size the pump displacement. Since Butch does not have an onboard HPU, there is no direct mechanical analog for modeling. Instead, the pump can be sized based on a nominal flow rate, Q_0, and nominal shaft speed, N_0, that represents the baseline performance. Equation (5.12) can then be used to estimate the pump displacement required to meet this baseline. The volumetric efficiency can be approximated with an assumed value of 0.7.

With an estimate of the pump displacement in hand, the pump geometry used for modeling the motor load coefficient. Approximating the displacement as half the volume of the annulus between the gear root diameter and the outer diameter, the displacement can be modeled as

$$D = \pi w\left[\left(r_p + a\right)^2 - \left(r_p - b\right)^2\right] \tag{5.15}$$

where w is the width of the gear, r_p is the gear pitch radius, a is the addendum, and b is the dedendum. Note that the one-half term from the gear annulus is canceled by having two gears contribute to pump displacement. In order to reduce the degrees of freedom to the displacement, the assumption is made that the gears will be geometrically similar regardless of pump size. This allows the gear parameters to be defined as a function of a single parameter, using the geometry of a previous gear from MeRLIn as a template. The ratios uses are below.

$$a = b = 0.1 r_p \tag{5.16}$$

$$w = 1.25 r_p \tag{5.17}$$

The pitch radius can then be estimated from the nominal displacement using Equation (5.15).

$$r_p = \left(\frac{2D}{\pi}\right)^{1/3} \tag{5.18}$$

The load torque for the motor model can also be defined using the same method.

$$c_L = \frac{1}{2\pi} D \tag{5.19}$$

The moment of inertia of the pump gears can be approximated as two cylinders with the same height and diameter as the gears.

$$J_{pump} = 2\frac{1}{2} m r_p^2$$

$$= \left(\rho\pi r_p^2 w\right) r_p^2$$
$$= \frac{5}{4}\rho\pi r_p^5 \tag{5.20}$$

5.3 Manifold

Fluid flow produced by the pump is supplied to the servo valves through the manifold. The supply pressure within the manifold, p_S, is a function of the balance of the fluid flux into and out of the manifold, the volume of the manifold, V_m, and the bulk modulus of the fluid used, β.

$$\frac{dp_S}{dt} = \frac{\beta}{V_m}(Q - Q_{RV} - Q_{in}) \tag{5.21}$$

In the above equation, Q is the supplied flow from the pump, Q_{RV} is the flowrate through the pressure relief valve, and Q_{in} is the sum of all flows into the 12 servo valve/actuator pairs.

5.4 Relief Valve

The relief valve is assumed to take the form of a spring-loaded poppet valve with a conical poppet seat. The relief valve is characterized by a spring stiffness, k, and effective damping b; the angle of the valve seat is α, and the diameter of the poppet is d_p. The position of the poppet, x, is defined such that the valve is fully closed at x = 0. A cross section of a nominal relief valve is shown below in Figure 5-2.

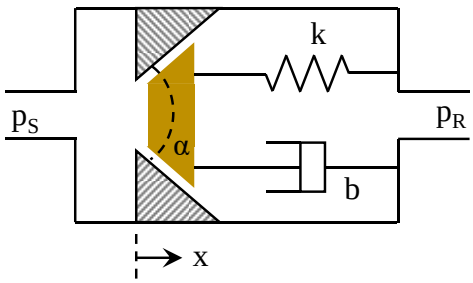

Figure 5-2. Cross section of the nominal relief valve.

The flow rate through the valve can be modeled using the orifice flow equation,

$$Q_{RV} = A_o c_d \sqrt{\frac{2(p_S - p_R)}{\rho}} \tag{5.22}$$

where A_o is the valve orifice area, c_d is the discharge coefficient, p_S is the supply pressure in the manifold, and p_R is the reservoir pressure. The orifice area equation is taken from the Matlab Simulink poppet valve model, shown below.

$$A_o = \begin{cases} A_{leak} & x \le 0 \\ \pi\left[d_p + x\sin\left(\frac{\alpha}{2}\right)\cos\left(\frac{\alpha}{2}\right)\right] x\sin\left(\frac{\alpha}{2}\right) + A_{leak} & 0 < x < x_{max} \\ A_{\max} + A_{leak} & x \ge x_{max} \end{cases} \tag{5.23}$$

A_{leak} is the effective leakage area of the poppet when seated, and A_{max} is the maximum area of the orifice when the valve is fully open at $x = x_{max}$, defined below.

$$A_{max} = \frac{\pi d_p^2}{4} \tag{5.24}$$

$$x_{max} = \frac{d_p}{\sin\alpha}\left(\sqrt{1+\cos\frac{\alpha}{2}} - 1\right) \tag{5.25}$$

For simplicity, it is assumed that the relief valve has negligible leakage, allowing us to set A_{leak} to zero.

The dynamics of the poppet valve are given by a simple force balance,

$$m\ddot{x} + b\dot{x} + kx = A_p(p_S - p_R) - F_p \tag{5.26}$$

where F_p is the preset spring load that sets the cracking pressure. To simplify the model, the poppet mass and damping coefficient are assumed to be negligible compared to the spring stiffness. This reduces Equation (5.26) to a time-invariant relation between the pressure load and poppet position.

$$x = \frac{1}{k}\left[A_p(p_S - p_R) - F_p\right] \tag{5.27}$$

The preset load is related to the cracking pressure, p_c.

$$F_p = \frac{\pi d_p^2}{4}(p_c - p_R) \tag{5.28}$$

In the above equation, the difference in area of the two sides of the poppet are assumed to be negligible, which is reasonable for supply pressures sufficiently large as expected in nominal operation ($p_c >> p_R$).

5.5 Valve Array

A model for the dynamics of the servo valve and actuator was developed in the MeRLIn program for simulating the performance of the Single Actuator Testbed.[5] While that work was useful for determining the characteristic equation of state for a valve-actuator pair, it relied on a linearization approximation. This linearization, while useful for linearized control implementation as done in

MeRLIn, is less useful for a deterministic computational model of a hydraulic system as it introduces error when operating away from the nominal operating conditions. Instead, the valve and actuator dynamics are modeled through separate functions that interface with each other.

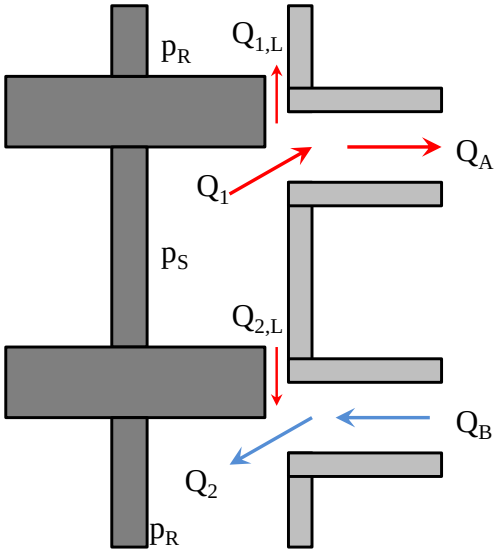

Figure 5-3. Metering orifice flows.

A similar geometry from the MeRLIn model is used, shown in Figure 5-3, where there are two metered orifice flows of interest, Q_A and Q_B, which correspond to ports A and B of the servo valve, respectively. Here we choose to define the convention that flow *out* of the valve through port A is positive, while flow *into* the valve through port B is positive. The flow through a metering orifice is a function of the pressure drop across the orifice, Δp, and the orifice area, A_o,

$$Q = c_d A_o \sqrt{\frac{2}{\rho}\Delta p} \tag{5.29}$$

where c_d is the discharge coefficient and ρ is the fluid density. The flow through the valve port is then the difference between the orifice flow and spool leakage flow. However, we shall assume negligible spool leakage flow through the valve port as the orifice flow rate. Thus, the flow rates can be written as

$$Q_A = c_d A_o \sqrt{\frac{2}{\rho}|p_S - p_A|}\, sign(p_S - p_A) \tag{5.30}$$

$$Q_B = c_d A_o \sqrt{\frac{2}{\rho}|p_B - p_R|}\, sign(p_B - p_R) \tag{5.31}$$

where the sign function is used to determine flow direction following the convention defined above.

The orifice area is a function of the orifice width, w_o, and the orifice opening, x.

$$A_o = \int_0^x w_o(z)dz \tag{5.32}$$

For a simple orifice design where the width is constant, the orifice area can be simplified.

$$A_o = w_o x \tag{5.33}$$

The orifice opening is a function of the torque motor current and orifice geometry, and in practice the flow-current profile can be unique for a given valve (due to dead bands, asymmetry in response, etc.). For simplicity, an ideal valve torque motor is assumed with a symmetric current-flow profile and no dead band. The orifice opening is then simply a linear relation to the torque motor current.

$$x = c_I I \tag{5.34}$$

Defining the overall valve gain, K_V, as

$$K_V = c_d c_I w_o \tag{5.35}$$

we can rewrite the valve flows as

$$Q_A = K_V I \sqrt{\frac{2}{\rho}|p_S - p_A|}\, sign(p_S - p_A) \tag{5.36}$$

$$Q_B = K_V I \sqrt{\frac{2}{\rho}|p_B - p_R|}\, sign(p_B - p_R) \tag{5.37}$$

where the value of K_V can be calculated from existing valve flow gain data. For this work, the valve flow gain data for the Moog Direct Drive Valve (DDV) is used.

5.6 Actuators

The linearized approximation used in the MeRLIn actuator model combined the dynamics of each valve with the paired actuator. This allowed for the problem to be defined as a system of linear equations that defined a differential state vector (composed of four state parameters) as a function of a coefficient matrix (primarily composed of the actuator and valve geoemetry), the state vector, and vector of operating conditions. While convenient to solve, this approach is only an approximation of the dynamics, and thus introduces error. However, a similar approach can be used that calculates a

differential state parameter as a function of the current state parameter and additional external operating conditions, though it will not be in a convenient form of linear equations.

The same conceptual actuator geometry from the MeRLIn model is used, illustrated below in Figure 5-4. The position of the piston, *y*, is defined such that the zero point is when the actuator is centered, and positive displacement extends the piston rod. Maintaining the flow convention from Section 5.5, Q_A is positive when fluid flows into the actuator, while Q_B is positive when fluid flows out of the actuator. The load force, F_L, is defined to be positive when it pushes against the piston (i.e. the actuator is pushing, not pulling).

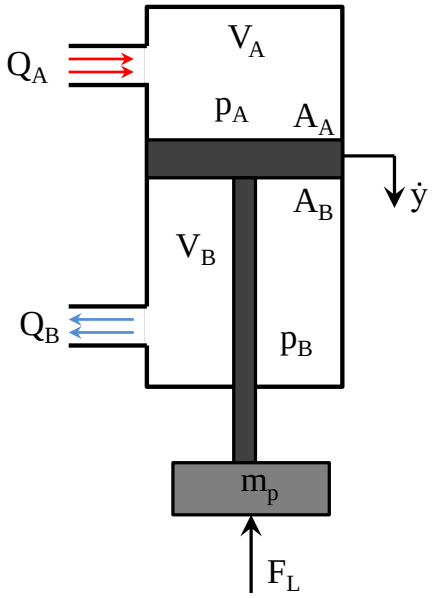

Figure 5-4. Conceptual actuator model.

The net force of the actuator on the load is the difference of the two chamber pressures multiplied against the corresponding piston area,

$$F_{act} = \eta_{act}(p_A A_A - p_B A_B) \tag{5.38}$$

where η_{act} is the actuator efficiency. The time rate of change of pressure in a volume of fluid is

$$\frac{dp}{dt} = \frac{\beta}{V}\left(Q_{in} - \frac{dV}{dt}\right) \tag{5.39}$$

where V is the volume of the fluid, β is the fluid bulk modulus, and Q_{in} is the net flow rate of fluid into the volume. The volume of each chamber of the actuator is a function of the actuator position relative to the nominal limits of the actuator range.

$$V_A = V_{A,0} + A_A(y - y_{min}) \tag{5.40}$$

$$V_B = V_{B,0} + A_B(y_{max} - y) \tag{5.41}$$

The rate of change of each chamber pressure can then be calculated as a function of actuator velocity and position.

$$\dot{p}_A = \frac{\beta}{V_A}(Q_A - A_A\dot{y}) \tag{5.42}$$

$$\dot{p}_B = \frac{\beta}{V_B}(-Q_B + A_B\dot{y}) \tag{5.43}$$

The net force on the actuator piston can be modeled as the vector sum of the pressure forces, frictional damping, and external forces,

$$F_{net} = \eta_{act}(p_A A_A - p_B A_B) - c_{act}\dot{y} - F_L + F_r \tag{5.44}$$

where c_{act} is the damping coefficient of the actuator, and F_r is the reaction force of the actuator stops against the piston when the actuator is fully extended or retracted. The stop is assumed to be a softer material that acts within its elastic range such that the reaction force is linear with axial compression.

$$F_r = -k\Delta y \tag{5.45}$$

The stiffness of the stop can be modeled using Young's modulus, E, which relates material stress, σ, and strain, ε.

$$E = \frac{\sigma}{\varepsilon} \tag{5.46}$$

If we assume the stop is an annular disc with outer diameter d_i, inner diameter d_i, and thickness t, the reaction force can be modeled as the material stress multiplied over the area of the stop.

$$\begin{aligned} F_r &= \sigma A \\ &= (\varepsilon E)A \\ &= \left(\frac{\Delta y}{t}\right)EA \\ F_r &= \frac{\pi}{4t}(d_o^2 - d_i^2)E\Delta y \end{aligned} \tag{5.47}$$

Thus we can approximate the piston stop stiffness as

$$k = \frac{\pi}{4t}(d_o^2 - d_i^2)E \tag{5.48}$$

and the reaction force based on the piston position.

$$F_r = \begin{cases} -k(y_{min} - y) & if\ y < y_{min} \\ -k(y - y_{max}) & if\ y > y_{max} \\ 0 & otherwise \end{cases} \tag{5.49}$$

It is useful for the function that captures the behavior of the actuators to calculate a differential change of a state variable as a function of the current state variable and current operating conditions. This allows for calculation of the differential change in the state variable and then integration across a time step to determine the new values for the state variable. In this case a similar setup is used from the MeRLIn model, where for each actuator the state variables are actuator speed, actuator position, pressure in chamber A, and pressure in chamber B. Using a change of variable for the actuator velocity,

$$\nu = \dot{y} \tag{5.50}$$

we can write the differential state equations.

$$\dot{\nu} = \frac{1}{m_p}[\eta_{act}(p_A A_A - p_B A_B) - c_{act}\dot{y} - F_L + F_r] \tag{5.51}$$

$$\dot{y} = \nu \tag{5.52}$$

$$\dot{p}_A = \frac{\beta}{V_A}(Q_A - A_A\dot{y}) \tag{5.53}$$

$$\dot{p}_B = \frac{\beta}{V_B}(-Q_B + A_B\dot{y}) \tag{5.54}$$

5.7 Reservoir

In order to close the system, the reservoir pressure must be modeled. This is due to the difference in actuator flow due to the presence of the piston rod. For systems with large reservoirs, this can be simplified with a constant pressure assumption. However, since the mobile HPU designed for Butch is sized to fit within mass limitations, the fluid volume of the reservoir is relatively small (within an order of magnitude of total fluid in the manifold and actuators). As such, the dynamics of the reservoir pressure must be modeled. The reservoir is modeled after the reservoir designed for the Butch HPU in MeRLIn,[6] with a rod-less piston/cylinder configuration, shown below in Figure 5-5. One side of the cylinder is fluid-filled, while the other is sealed and filled with pressurized gas. The reservoir has a nominal starting condition where the two compartment volumes have initial values of V_f and V_g for the fluid and gas volumes, respectively. The both volumes begin at an initial pressure of p_{g0}. The position of the piston, *z*, is defined such that $z = 0$ when the piston is fully extended against the fluid side, and positive *z* is towards the gas side.

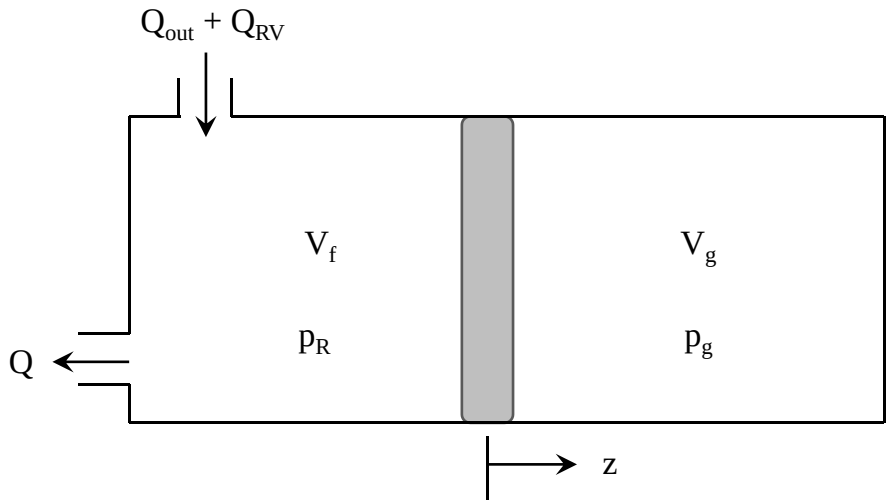

Figure 5-5. Reservoir model. Left side of the reservoir is fluid-filled, while the right side is pressurized gas.

Flow out of the reservoir is *Q*, the flow rate driven by the pump; flow into the reservoir is the sum of the flow rate out of the valve-actuator pairs and the flow through the relief valve, Q_{out} and Q_{RV} respectively. The piston is modeled as starting at the midpoint of the reservoir such that $V_{f0} = V_{g0}$. This is also the zero-point of the piston's axis of motion, *z*, and is the nominal position for the purposes of linearization. The piston has an area denoted by A_R.

The pressure in the fluid portion of the reservoir, p_R, is a function of the change in volume of the reservoir and the net flow rate into the reservoir.

$$\frac{dp_R}{dt} = \frac{\beta}{V_f}(Q_{out} + Q_{RV} - Q - A_R\dot{z}) \tag{5.55}$$

The pressure in the gas compartment is modeled assuming an ideal gas,

$$p_g V_g = nR_u T \tag{5.56}$$

where *n* is the number of moles of the gas, R_u is the universal gas constant, and *T* is the gas temperature. If isothermal conditions are assumed (which is reasonable in the absence of large piston displacements), the right hand side of the equation is constant and can be lumped into the term k_0 calculated from the initial gas pressure and volume.

$$k_0 = nR_u T = p_{g,i} V_{g,i} \tag{5.57}$$

The time rate of change of the gas pressure can be found from the derivative of Equation (5.56).

$$\frac{dp_g}{dt} = k_0 \frac{d}{dt}\left(\frac{1}{V_g}\right)$$

$$= k_0 \frac{d}{dt}\left(\frac{1}{V_{g0} - A_R z}\right)$$

$$= k_0 \frac{A_R \frac{dz}{dt}}{\left(V_{g0} - A_R z\right)^2} \tag{5.58}$$

The force equation for the piston is then

$$m_p \ddot{z} + b\dot{z} = A_R\left(p_R - p_g\right) \tag{5.59}$$

Using a change of variables,

$$\dot{z} = \psi \tag{5.60}$$

the reservoir can be modeled using the same approach used for the actuator, where the differential state variables can be solved as a function of the current state variables and operating conditions.

$$\dot{\psi} = \frac{1}{m_p}\left[\eta_{act} A_R\left(p_R - p_g\right) - b\psi + F_r\right] \tag{5.61}$$

$$\dot{z} = \psi \tag{5.62}$$

$$\dot{p}_R = \frac{\beta}{V_f}\left(Q_R + Q_{RV} - Q - A_R\psi\right) \tag{5.63}$$

$$\dot{p}_g = \frac{k_0}{V_g^2} A_R \psi \tag{5.64}$$

Note that the convention is that positive Q_R and Q_{RV} is flow into the reservoir from the return side of the valves and the relief valve, respectively, and positive Q is flow out of the reservoir to the pump. The volume of the two sides of the reservoir can be calculated based on the reservoir piston location and the starting position of the piston, z_0.

$$V_f = V_{f,0} + A_R z \tag{5.65}$$

$$V_g = V_{g,0} - A_R(L - z) \tag{5.66}$$

The terms $V_{f,0}$ and $V_{g,0}$ denote the corresponding reservoir volumes when the piston is fully extended towards either end. These parameters include additional volume beyond the limits of the piston, such as space within the piston, the cylinder, or, as in the case of the Butch HPU, within the manifold itself. The initial gas condition constant, k_0, can then be calculated based on the initial position of the piston and the initial gas pressure.

$$k_0 = p_{gi}\left(V_{g,0} + A_R(L - z_i)\right) \tag{5.67}$$

The reaction force of the reservoir piston against the reservoir cylinder ends is modeled in the same manner as the actuator, with an annular ring of contact dictated by the piston shape. The stiffness of the piston head is determined by

$$k = \frac{\pi}{4t}(d_o^2 - d_i^2)E \tag{5.68}$$

where the thickness, *t*, is the thickness of the piston, and the inner and outer diameters are that of the area of contact. With the established convention that $z = 0$ when the piston is at initial contact with the cylinder at the fluid port end, the reaction force can be written as follows.

$$F_r = \begin{cases} -kz & if\ z < 0 \\ -k(z - L) & if\ z > L \\ 0 & otherwise \end{cases} \tag{5.69}$$

6.0 Hydraulic Model Implementation

6.1 Model Overview

The model is constructed in Matlab Simulink as an interconnected set of embedded Matlab functions that model each subsystem. The model assumes 12 servo valves and 12 actuators, mimicking the Butch quadruped configuration. The inputs to the model are the applied motor voltage, a 12-element array of valve current commands, and a 12-element array of actuator load forces. There are six top-level constants: the fluid density, ρ, and bulk modulus, β; the manifold filter hydraulic resistance, $R_{h,f}$, and the relief valve cracking pressure, p_c; the two pump sizing parameters are the required flow rate, Q_{req}, and the nominal pump speed, N_0. The outputs of the function are the motor torque, the motor speed, the flow rate supplied to the valves, the flow rate through the relief valve, the pump discharge pressure, the valve supply pressure, the return pressure, and the 4x12 actuator state matrix VAS. The VAS matrix includes the actuator velocity, position, and pressure in each chamber for all 12 actuators. The Simulink block diagram of the model is shown below in Figure 6-1.

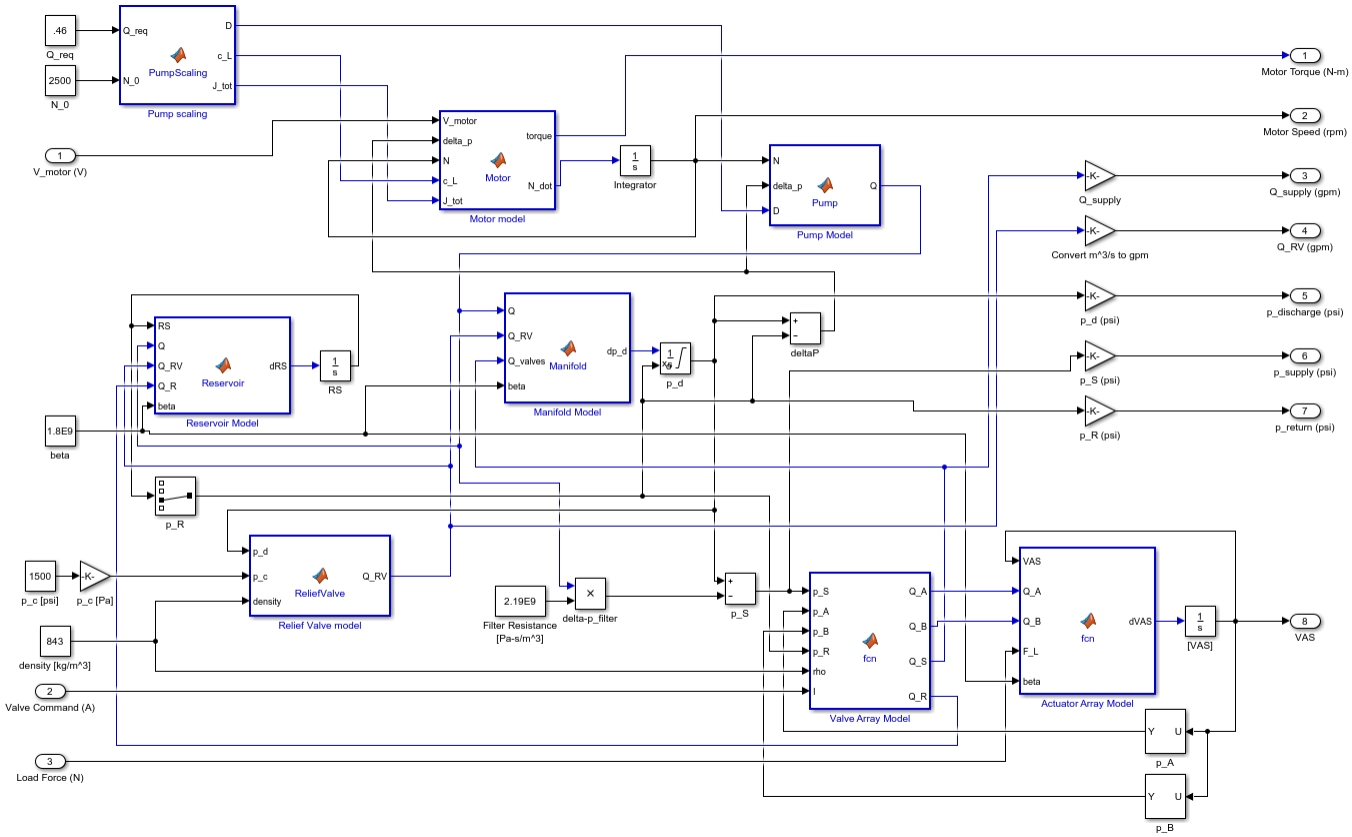

Figure 6-1. Hydraulic model in Simulink.

There are four integrators used in the hydraulic model. The first is used to integrate the time rate of change of the motor speed, the second integrates the time rate of change of the supply pressure in the manifold, the third is for the integration of the time rate of change of the 4x12 state matrix of the system of valve-actuator pairs, and the final integrator is for the 4-element state vector of the reservoir. The initial conditions of these integrators are shown below in Table 5. Note that the initial condition for the discharge pressure is defined to be the same as the initial reservoir pressure, RS(3). Note that pressures in Table 5 are given in bar for formatting, and that 1 bar is 100,000 Pa.

Table 5. Integrator Initial Conditions

N	0 rpm
p_d	300,000 Pa
RS	[0 m/s; 0.04 m; 3 bar; 3 bar]
VAS	$\begin{bmatrix} 0\ 0\ 0\ 0\ 0\ 0\ 0\ 0\ 0\ 0\ 0\ 0 \\ 0\ 0\ 0\ 0\ 0\ 0\ 0\ 0\ 0\ 0\ 0\ 0 \\ 3\ 3\ 3\ 3\ 3\ 3\ 3\ 3\ 3\ 3\ 3\ 3 \\ 3\ 3\ 3\ 3\ 3\ 3\ 3\ 3\ 3\ 3\ 3\ 3 \end{bmatrix} \begin{bmatrix} m/s \\ m \\ bar \\ bar \end{bmatrix}$

The supply pressure to the valves is calculated assuming a constant hydraulic resistance of the manifold filter.

$$p_d = p_s + QR_{h,f} \tag{6.1}$$

This assumes that the filter is placed in parallel with the relief valve and before the valves, as is the case in the Butch HPU. One reason for this is that the relief valve being upstream of the filter to manages the risk of a clogged filter leading to excessive manifold pressure.

Each embedded Matlab function calculates either the time rate of change of the parameter of interest or directly solves for the parameter of interest according to the characteristic equation derived in Section 5.0. Sub-component constants, such as valve gains or motor constants, are defined within the corresponding Matlab functions to minimize clutter within the overall model, and is covered in Section 6.2.

6.2 Component Geometry & Assumptions

While the model calculates the state variables of the different subsystems, there are multiple geometric or performance parameters that are referenced, measured, empirically calculated, or outright assumed. The parameters used in the model that are not explicitly calculated are given in the tables below, grouped by subsystem.

6.2.1 Pump

In order to facilitate a wide range of possible operating conditions without requiring the fine details of all possible pump geometries simulated, a pump scaling function is used to estimate the relevant pump parameters, such as displacement or torque load at a given pressure. This pump scaling function is not a deterministic function, but rather an empirical approximation of pump performance across a range of possible flow rates. The function takes in a desired flow rate and a nominal pump speed for that flow rate. The function then calculates the pump and motor parameters needed. There are several assumed values, such as the density of the gear material and the moment inertia of the motor, shown below in Table 6.

Table 6. Assumed Pump Scaling Parameters

η_v	0.85
ρ_{gear}	7750 kg/m^3
J_{motor}	3.147x10^{-4} kg-m^2

The assumed value for the motor moment of inertia is set by the selected motor, which is not scaled by this function. This value should be set by the simulated motor specification. This value currently used is from empirical measurements of motor speed during the MeRLIn program of the motor being simulated, discussed below.

Most of the pump performance parameters are determined using the pump scaling function, except for two: the pump constants R_G and $\mathbb{R}_G$. These two parameters reflect the inter-component spacing within the pump that constitute the leakage pathway from pump discharge to pump suction, and can be approximated as constant across a limited range of pump displacements. Note that for very large changes in pump displacement this approximation does not hold, but for systems of a size similar to the Butch HPU, this is sufficiently accurate. This simplification is made due to the difficulty in calculating these constants, and the values used in the model are based on empirical data from the MeRLIn MkIIIc gear pump.

Table 7. Pump Constants

R_G	1.0x10^{12} Pa-s/m^3
$\mathbb{R}_G$	100x10^6 m^{-3}

6.2.2 Motor

The motor parameters are taken from measurements of the motor used in the MeRLIn program, Alien Power Systems 5065 BLDC motor, 150K_V.

Table 8. Motor Parameters

K_T	0.078 N-m/A
R_{LL}	0.165 Ohms
b_m	7.14x10^{-6} N-m-s/rad
b_p	1x10^{-3} N-m-s/rad
I_{max}	50 A

6.2.3 Manifold

The manifold volume is estimated from a CAD model of the Butch HPU manifold passages between the pump discharge and the relief valve and the discharge filter. The model uses a manifold volume of 4.83x10^{-6} m^3.

6.2.4 Relief Valve

The parameters of the relief valve are approximated using a stock relief valve used in MeRLIn hydraulic tests.

Table 9. Assumed Relief Valve Parameters

k	$5.16x10^{4}$ N/m
d_p	$6.35x10^{-3}$ m
α	$2\pi/3$ rad
C_d	0.78

6.2.5 Servo Valves

The main parameter of interest for the valves is the valve gain, which relates the flow through the controlling orifice for a given pressure drop and current command. The valve gain was estimated using valve performance measurements made on the Moog Direct Drive Valve during the MeRLIn program. It is worth repeating that this model assumes no dead band on the valve and a symmetric flow response. Each valve is likely to be unique in its flow response, so this approximation is still idealistic.

6.2.6 Actuators

The actuators are modeled after those developed in-house at NRL for the MeRLIn program and integrated into the Butch quadruped. While the values taken are not exact matches, they are similar. The actuator stop stiffness assumes a hard rubber with a Young's modulus of 40 MPa. A damping coefficient of 10 is assumed to represent the seals on both the piston head and the rod.

Table 10. Assumed Actuator Parameters

k	$1.436x10^{6}$ N/m
m_p	0.05 kg
y_{max}	0.035 m
y_{min}	-0.035 m
η_{act}	0.95
A_A	$7.13x10^{-5}$ m^2
A_B	$5.35x10^{-5}$ m^2
$V_{A,0}$	$6.5x10^{-7}$ m^3
$V_{B,0}$	$6.5x10^{-7}$ m^3
c	10

6.2.7 Reservoir

The reservoir is modeled after the Butch HPU reservoir developed at the end of the MeRLIn project. The relevant geometric parameters are given below in Table 11. The piston stiffness, *k*, is calculated assuming AL6061 material properties. An initial gas pressure of 3 bar is assumed. A damping coefficient of 10 is assumed, similar to the actuators.

Table 11. Reservoir Parameters

L	0.0635 m
A_R	0.00115 m^2
$V_{f,0}$	$2.30x10^{-5}$ m^3
$V_{g,0}$	$2.30x10^{-5}$ m^3
z_i	0.04 m
m_p	0.040 kg
k	$1.42x10^{12}$ N/m
b	10

6.3 Subsystem Function Code

Below is the Matlab code for each subsystem function.

6.3.1 Pump Scaling

```
function [D, c_L, J_tot] = PumpScaling(Q_req, N_0)
%Sizes the pump based on specified required flow rate and a nominal speed.
%The function then defines the torque constant of the pump and the total
%moment of inertia.

%Units of input parameters:
%[Q_req] = gpm
%[N_0] = rpm

%Assumptions and Constants
%Additional geometric assumptions made, see writeup for derivation
eta_v = 0.85;                               %assume constant volumetric efficiency
rho = 7750;                                 %density of the gears (17-4 ph SS) [kg/m^3]
J_motor = 0.0003147;                        %Estimated moment of inertia of the motor [kg-m^2]

%Calculations
D = 60*Q_req / (15852*eta_v*N_0);           %Pump displacement [m^3]
r_p = (2*D/pi)^(1/3);                       %Gear pitch radius [m]
c_L = (1/2)*D/pi;                           %Pump torque constant [N-m/Pa] = [m^3]
J_tot = (5/4)*pi*rho*r_p^5 + J_motor;       %Moment of inertia (pump + motor) [kg-m^2]
end
```

6.3.2 Motor Model

```
function [torque, N_dot] = Motor(V_motor, delta_p, N, c_L, J_tot)
% Embedded Matlab script to solve for dN/dt as a function of state
```

```
%Motor Constants
K_T = 0.078;         %motor torque constant [N-m/A]
R_LL = 0.165;        %motor line-line resistance [Ohms]
b_m = 7.14E-6;       %motor damping [N-m/rad/s]
b_p = 1E-3;          %pump damping from friction [N-m/rad/s]
I_max = 50;          %maximum line current possible [A]

%Calculations
K_e = (2*pi/60)*sqrt(2/3)*K_T;      %Motor emf constant [V/rpm]
torque = K_T/R_LL*(V_motor-K_e*N);

if torque > I_max*K_T               %Check to see if motor torque exceeds maximum allowable
    torque = I_max*K_T;
end

N_dot = 60/(2*pi*J_tot) *(torque - 2*pi/60*(b_m+b_p)*N - c_L*delta_p);
end
```

6.3.3 Pump Model

```
function Q = Pump(N, delta_p, D)
%Gear pump model; uses the gear resistance formulation.  Primary assumption is that
%gear resistance and gear reluctance is independent of pump scaling, i.e. that
%machining and assembly tolerances are independent of component size.

%units
%[N] = rpm
%[delta_p] = Pa

%Assumptions and constants
R_G = 1000 * 10^9;                      %Gear resistance [Pa-s/m^3]
RR_G = 100*10^6;                        %Gear reluctance [1/m^3]

%Calculations
Q = (N/60)*(D-1/RR_G) - delta_p/R_G;    %Pump output flow rate [m^3/s]
end
```

6.3.4 Manifold Model

```
function dp_d = Manifold(Q, Q_RV, Q_valves, beta)
%Model of the pressure dynamics in the manifold

%Constants
V_m = 4.83E-6;               %Manifold volume [m^3]

dp_d = beta/V_m*(Q - Q_RV - Q_valves);
end
```

6.3.5 Relief Valve Model

```
function Q_RV = ReliefValve(p_d, p_c, density)
%Model of a spring-loaded poppet-style relief valve

%Constants and assumptions
k = 5.16E4;                     %Preload spring stiffness [N/m]
d_p = 6.35E-3;                  %Poppet diameter [m]
alpha = 2*pi/3;                 %Poppet angle
C_d = 0.78;                     %discharge coefficient

%Calculations
c_o = pi*d_p^2/(4*k)*sin(alpha/2);          %Orifice constant [m^3/N]
```

```
%Determine orifice area based on cracking pressure
if (p_d > p_c)
    A_o = pi*d_p*c_o*(p_d - p_c) + pi*cos(alpha/2)*c_o^2*(p_d - p_c)^2;     %Orifice area
[m^2]
else
    A_o = 0;
end

%Ensure that a negative pressure does not introduce imaginary number
if p_d < 0
    Q_RV = 0;
else
    Q_RV = A_o*C_d*sqrt(abs(2*p_d/density));
end

end
```

6.3.6 Valve Array Model

```
function [Q_A, Q_B, Q_S, Q_R] = fcn(p_S, p_A, p_B, p_R, rho, I)
%This models flow through the spool valves (array of 12 valves). Input
%parameters are: supply pressure (scalar), pressure at port A (array of
%12), pressure at port B (array of 12), return pressure (scalar), fluid
%density, and valve command currents (array of 12).  Outputs are: flow
%rates through ports A (array of 12), flow through ports B (array of 12),
%total supply flow rate (scalar) and total return flow rate (scalar)

%Valve definitions
K_V = zeros(1,12);          %initialize array of valve gains

for i = 1:12                %assign individual valve gains
    K_V(i) = [REDACTED]      %[m^2/A]
end

%Initialize outputs
Q_S = 0;
Q_R = 0;
Q_A = zeros(1,12);
Q_B = zeros(1,12);
Q_S = 0;
Q_R = 0;

%Calculate valve flows
for i = 1:12

    %Calculates flow rates based on current command (spool position)
    if I(i)>=0
        %Frame of reference condition; positive Q_A is out of valve into
        %the actuator, positive Q_B is out of the actuator into the valve
        Q_A(i) = K_V(i)*I(i)*sqrt(2/rho*abs(p_S-p_A(i)))*sign(p_S-p_A(i));
        Q_B(i) = K_V(i)*I(i)*sqrt(2/rho*abs(p_B(i)-p_R))*sign(p_B(i)-p_R);

        Q_S = Q_S + Q_A(i);
        Q_R = Q_R + Q_B(i);
    else
        %Opposite condition from reference frame; negative Q_A denotes flow
        %coming from the actuator into the valve, and negative Q_B denotes
        %flow from the valve to the actuator

        %Note: minus sign due to flow direction convention
        Q_A(i) = K_V(i)*I(i)*sqrt(2/rho*abs(p_A(i)-p_R))*sign(p_A(i)-p_R);
```

```
        Q_B(i) = K_V(i)*I(i)*sqrt(2/rho*abs(p_S-p_B(i)))*sign(p_S-p_B(i));

        Q_S = Q_S - Q_B(i);
        Q_R = Q_R - Q_A(i);
    end
end
```

6.3.7 Actuator Array Model

```
function dVAS = fcn(VAS, Q_A, Q_B, F_L, beta)
%This model is the hydraulic portion of the valve-actuator dynamics that couples with
%the kinematic model.  VAS stands for Valve-Actuator State, which contains all
%information about the state of the valve-actuator system
%VAS(i) = [nu; y; p_A; p_B]
%dVAS(i) = [nu_dot; y_dot; p_Adot; p_Bdot]

%I and F_L are 12 element vectors corresponding to each actuator valve pair, where
%I is the command current, and F_L is the load force determined by the kinematic model

%Definition and initialization
c_act = zeros(1,12);
m_p = zeros(1,12);
eta_act = zeros(1,12);
A_A = zeros(1,12);
A_B = zeros(1,12);
V_A = zeros(1,12);
V_B = zeros(1,12);
V_A0 = zeros(1,12);
V_B0 = zeros(1,12);
y_max = zeros(1,12);
y_min = zeros(1,12);
k = zeros(1,12);
F_r = zeros(1,12);
dVAS = zeros(4,12);

%Actuator 1:
c_act(1) = 10;                          %actuator damping coefficient
m_p(1) = 0.05;                           %Actuator piston head mass [kg]
y_max(1) = 0.035;                        %maximum position [m]
y_min(1) = -0.035;                       %minimum position [m]
eta_act(1) = 0.95;                       %Actuator efficiency
A_A(1) = 7.13E-5;                        %Actuator side A piston area [m^2]
A_B(1) = 0.75*A_A(1);                    %Actuator side B piston area [m^2]
V_A0(1) = 6.5E-7;                        %Minimum volume of chamber A [m^3]
V_B0(1) = 6.5E-7;                        %Minimum volume of chamber B [m^3]
k(1) = 1.436e6;                          %Actuator stop stiffness [N/m]

%Actuator 2:
c_act(2) = 100;                         %actuator damping coefficient
m_p(2) = 0.05;                           %Actuator piston head mass [kg]
y_max(2) = 0.035;                        %maximum position [m]
y_min(2) = -0.035;                       %minimum position [m]
eta_act(2) = 0.95;                       %Actuator efficiency
A_A(2) = 7.13E-5;                        %Actuator side A piston area [m^2]
A_B(2) = 0.75*A_A(2);                    %Actuator side B piston area [m^2]
V_A0(2) = 6.5E-7;                        %Minimum volume of chamber A [m^3]
V_B0(2) = 6.5E-7;                        %Minimum volume of chamber B [m^3]
k(2) = 1.436e6;                          %Actuator stop stiffness [N/m]

%Actuator 3:
c_act(3) = 100;                         %actuator damping coefficient
m_p(3) = 0.05;                           %Actuator piston head mass [kg]
y_max(3) = 0.035;                        %maximum position [m]
```

```
y_min(3) = -0.035;                  %minimum position [m]
eta_act(3) = 0.95;                  %Actuator efficiency
A_A(3) = 7.13E-5;                   %Actuator side A piston area [m^2]
A_B(3) = 0.75*A_A(3);               %Actuator side B piston area [m^2]
V_A0(3) = 6.5E-7;                   %Minimum volume of chamber A [m^3]
V_B0(3) = 6.5E-7;                   %Minimum volume of chamber B [m^3]
k(3) = 1.436e6;                     %Actuator stop stiffness [N/m]

%Actuator 4:
c_act(4) = 100;                    %actuator damping coefficient
m_p(4) = 0.05;                      %Actuator piston head mass [kg]
y_max(4) = 0.035;                   %maximum position [m]
y_min(4) = -0.035;                  %minimum position [m]
eta_act(4) = 0.95;                  %Actuator efficiency
A_A(4) = 7.13E-5;                   %Actuator side A piston area [m^2]
A_B(4) = 0.75*A_A(4);               %Actuator side B piston area [m^2]
V_A0(4) = 6.5E-7;                   %Minimum volume of chamber A [m^3]
V_B0(4) = 6.5E-7;                   %Minimum volume of chamber B [m^3]
k(4) = 1.436e6;                     %Actuator stop stiffness [N/m]

%Actuator 5:
c_act(5) = 100;                    %actuator damping coefficient
m_p(5) = 0.05;                      %Actuator piston head mass [kg]
y_max(5) = 0.035;                   %maximum position [m]
y_min(5) = -0.035;                  %minimum position [m]
eta_act(5) = 0.95;                  %Actuator efficiency
A_A(5) = 7.13E-5;                   %Actuator side A piston area [m^2]
A_B(5) = 0.75*A_A(5);               %Actuator side B piston area [m^2]
V_A0(5) = 6.5E-7;                   %Minimum volume of chamber A [m^3]
V_B0(5) = 6.5E-7;                   %Minimum volume of chamber B [m^3]
k(5) = 1.436e6;                     %Actuator stop stiffness [N/m]

%Actuator 6:
c_act(6) = 100;                    %actuator damping coefficient
m_p(6) = 0.05;                      %Actuator piston head mass [kg]
y_max(6) = 0.035;                   %maximum position [m]
y_min(6) = -0.035;                  %minimum position [m]
eta_act(6) = 0.95;                  %Actuator efficiency
A_A(6) = 7.13E-5;                   %Actuator side A piston area [m^2]
A_B(6) = 0.75*A_A(6);               %Actuator side B piston area [m^2]
V_A0(6) = 6.5E-7;                   %Minimum volume of chamber A [m^3]
V_B0(6) = 6.5E-7;                   %Minimum volume of chamber B [m^3]
k(6) = 1.436e6;                     %Actuator stop stiffness [N/m]

%Actuator 7:
c_act(7) = 100;                    %actuator damping coefficient
m_p(7) = 0.05;                      %Actuator piston head mass [kg]
y_max(7) = 0.035;                   %maximum position [m]
y_min(7) = -0.035;                  %minimum position [m]
eta_act(7) = 0.95;                  %Actuator efficiency
A_A(7) = 7.13E-5;                   %Actuator side A piston area [m^2]
A_B(7) = 0.75*A_A(7);               %Actuator side B piston area [m^2]
V_A0(7) = 6.5E-7;                   %Minimum volume of chamber A [m^3]
V_B0(7) = 6.5E-7;                   %Minimum volume of chamber B [m^3]
k(7) = 1.436e6;                     %Actuator stop stiffness [N/m]

%Actuator 8:
c_act(8) = 100;                    %actuator damping coefficient
m_p(8) = 0.05;                      %Actuator piston head mass [kg]
y_max(8) = 0.035;                   %maximum position [m]
y_min(8) = -0.035;                  %minimum position [m]
eta_act(8) = 0.95;                  %Actuator efficiency
A_A(8) = 7.13E-5;                   %Actuator side A piston area [m^2]
A_B(8) = 0.75*A_A(8);               %Actuator side B piston area [m^2]
V_A0(8) = 6.5E-7;                   %Minimum volume of chamber A [m^3]
```

```
V_B0(8) = 6.5E-7;                          %Minimum volume of chamber B [m^3]
k(8) = 1.436e6;                            %Actuator stop stiffness [N/m]

%Actuator 9:
c_act(9) = 100;                           %actuator damping coefficient
m_p(9) = 0.05;                             %Actuator piston head mass [kg]
y_max(9) = 0.035;                          %maximum position [m]
y_min(9) = -0.035;                         %minimum position [m]
eta_act(9) = 0.95;                         %Actuator efficiency
A_A(9) = 7.13E-5;                          %Actuator side A piston area [m^2]
A_B(9) = 0.75*A_A(9);                      %Actuator side B piston area [m^2]
V_A0(9) = 6.5E-7;                          %Minimum volume of chamber A [m^3]
V_B0(9) = 6.5E-7;                          %Minimum volume of chamber B [m^3]
k(9) = 1.436e6;                            %Actuator stop stiffness [N/m]

%Actuator 10:
c_act(10) = 100;                           %actuator damping coefficient
m_p(10) = 0.05;                             %Actuator piston head mass [kg]
y_max(10) = 0.035;                          %maximum position [m]
y_min(10) = -0.035;                         %minimum position [m]
eta_act(10) = 0.95;                         %Actuator efficiency
A_A(10) = 7.13E-5;                          %Actuator side A piston area [m^2]
A_B(10) = 0.75*A_A(10);                      %Actuator side B piston area [m^2]
V_A0(10) = 6.5E-7;                          %Minimum volume of chamber A [m^3]
V_B0(10) = 6.5E-7;                          %Minimum volume of chamber B [m^3]
k(10) = 1.436e6;                            %Actuator stop stiffness [N/m]

%Actuator 11:
c_act(11) = 100;                           %actuator damping coefficient
m_p(11) = 0.05;                             %Actuator piston head mass [kg]
y_max(11) = 0.035;                          %maximum position [m]
y_min(11) = -0.035;                         %minimum position [m]
eta_act(11) = 0.95;                         %Actuator efficiency
A_A(11) = 7.13E-5;                          %Actuator side A piston area [m^2]
A_B(11) = 0.75*A_A(11);                      %Actuator side B piston area [m^2]
V_A0(11) = 6.5E-7;                          %Minimum volume of chamber A [m^3]
V_B0(11) = 6.5E-7;                          %Minimum volume of chamber B [m^3]
k(11) = 1.436e6;                            %Actuator stop stiffness [N/m]

%Actuator 12:
c_act(12) = 100;                           %actuator damping coefficient
m_p(12) = 0.05;                             %Actuator piston head mass [kg]
y_max(12) = 0.035;                          %maximum position [m]
y_min(12) = -0.035;                         %minimum position [m]
eta_act(12) = 0.95;                         %Actuator efficiency
A_A(12) = 7.13E-5;                          %Actuator side A piston area [m^2]
A_B(12) = 0.75*A_A(12);                      %Actuator side B piston area [m^2]
V_A0(12) = 6.5E-7;                          %Minimum volume of chamber A [m^3]
V_B0(12) = 6.5E-7;                          %Minimum volume of chamber B [m^3]
k(12) = 1.436e6;                            %Actuator stop stiffness [N/m]

%-----------------dVAS Calculation---------
for i = 1:12
    %Preliminary calculations
    V_A(i) = V_A0(i) + A_A(i)*(VAS(2,i) - y_min(i));
    V_B(i) = V_B0(i) + A_B(i)*(y_max(i) - VAS(2,i));

    %Determine reaction force based on piston position; if the piston is
    %beyond the max or min, the reaction force is actuator stop stiffness
    %multipled by the distance beyond the limit in the opposite direction
    if VAS(2,i) < y_min(i)
        F_r(i) = -k(i)*(VAS(2,i) - y_min(i));
    elseif VAS(2,i) > y_max(i)
        F_r(i) = -k(i)*(VAS(2,i) - y_max(i));
    else
```

```
        F_r(i) = 0;
    end

    %Calculating dVAS terms
    dVAS(1,i) = 1/m_p(i)*(eta_act(i)*(A_A(i)*VAS(3,i)-A_B(i)*VAS(4,i))-c_act(i)*VAS(1,i)-
F_L(i)+F_r(i));
    dVAS(2,i) = VAS(1,i);
    dVAS(3,i) = beta/V_A(i)*(Q_A(i) - A_A(i)*VAS(1,i));
    dVAS(4,i) = beta/V_B(i)*(-Q_B(i) + A_B(i)*VAS(1,i));

end
end
```

6.3.8 Reservoir Model

```
function dRS  = Reservoir(RS, Q, Q_RV, Q_R, beta)
% Model for a dynamic gas-piston reservoir
%RS is the reservoir state array [z_dot; z; p_fluid; p_gas]

%Initialization
dRS = [0; 0; 0; 0];

%Constants & Definitions
b = 10;                             %Reservoir piston damping coefficient
A_R = 0.0011;                        %Piston area [m^2]
m_p = 0.04;                          %Piston mass [kg]
L = 0.0635;                          %Reservoir length [m]
V_f0 = 2.3e-5;                       %Nominal fluid volume [m^3]
V_g0 = 2.3e-5;                       %Nominal gas volume [m^3]
p_gi = 3*100000;                     %Initial gas pressure [Pa]
z_i = 0.04;                          %Initial piston position
k = 1.42e12;                         %piston axial stiffness [N/m]
k_0 = p_gi*(V_g0+A_R*(L-z_i));       %Gas constant for isothermal conditions

%Preliminary Calculations
V_f = V_f0 + A_R*RS(2);
V_g = V_g0 + A_R*(L-RS(2));

if RS(2) < 0
    F_r = -k*RS(2);
elseif RS(2) > L
    F_r = -k*(RS(2)-L);
else
    F_r = 0;
end

%Problem formulation
dRS(1) = 1/m_p*(A_R*(RS(3) - RS(4)) - b*RS(1) + F_r);
dRS(2) = RS(1);
dRS(3) = beta/V_f*(Q_R + Q_RV - Q - A_R*RS(1));
dRS(4) = k_0/V_g^2*A_R*RS(1);
end
```

7.0 Model Predictive Control Algorithm

The model predictive control (MPC) algorithm was developed to utilize analytical representations of the system to estimate state parameter outcomes. MPC is computationally intensive, but does not require empirical formulations or large state histories from which to determine the system behavior. One advantage of MPC is that it can be used in conjunction with a machine learning system to train the system virtually before risking the system in real-world conditions. This section attempts to formulate the current model predictive control strategy implemented in software. Algorithm (1) describes the sequence of steps taken to update the control law at each time step. The software is currently run in a Mujoco simulation named MPCTest. On each step, command and sensor inputs are passed to the robot object. Next, the step method is called. Finally, the joint torques are passed back to MPCTest where they are applied to the simulation dynamics specified by the loaded robot model. Section (2) briefly describes notation used throughout the document. Section (3) describes the system inputs. Sections (4)-(13) describe the sub-components of the algorithm, which correspond to the description in Algorithm(1).

Algorithm 1 Control Step Sequence

Input: Commands
Input: Sensors
Output: Joint torques
1: Estimate state
2: Run Walk state machine
3: Update gait pattern modulator
4: Run Leg state machine
5: Calculate desired foot placement
6: Generate base trajectory
7: Generate stance leg trajectories
8: Generate swing leg trajectories
9: Update stance leg controller
10: Update swing leg controller

7.1 Notation

$\mathbb{R}$	: set of real numbers
$\mathbb{I}$	: set of imaginary numbers
W	: world frame
B	: base frame
x_Y	: variable Y in frame x
x_{Ry}	: rotation matrix, frame y expressed in frame x

7.2 System Inputs

Command inputs are the inputs provided to the system representing the reference inputs and adjustable parameters to the control algorithms.

7.2.1 Variables

$H_{base} \in \mathsf{R}$	:	base height
$L_{span} \in \mathsf{R}$	:	step half length
$H_{sw} \in \mathsf{R}$	:	swing height
$v_d \in \mathsf{R}_6$	:	command velocity (twist)
$G_x \in \mathsf{R}_4$	:	gait pattern e.g. G_{trot}

7.2.2 Command Velocity

The desired linear and rotational rates provided to the system. Currently the z direction velocity, roll rate, and pitch rate are assumed to be zero.

7.2.3 Gait Pattern

The gait pattern input is a string or enum that specifies the desired gait pattern. The input is converted into phase lags for the gait pattern modulator.

7.2.4 Base Height

The desired height of the base.

7.2.5 Step Half Length

The one half of the desired foot stride length.

7.2.6 Swing Height

The desired maximum height of the foot when in the swing phase of a stride.

7.3 Sensor Inputs

Sensor inputs are the inputs provided to the system representing state feedback to the control algorithms.

7.3.1 Variables

$t \in \mathsf{R}_{\geq 0}$	:	current time step
$\mathbf{q}_{base} \in \mathsf{R} \times \mathsf{I}_3$	:	base orientation
$\Phi_{base} \in \mathsf{R}_3$	:	Euler angles
$\omega_{base} \in \mathsf{R}_3$	:	base angular velocity

$\ddot{p}_{base} \in R_3$	:	base acceleration
$q_r \in R_{12}$	:	joint positions
$\dot{q}_r \in R_{12}$	:	joint velocities
$f_c \in R_4$	:	contact force
$\dot{p}_{base} \in R_3$	:	base velocity
$p_{base} \in R_3$	:	base position

7.3.2 Timestep

Current time of CPU or Mujoco simulator.

7.3.3 Base Orientation

Quaternion of base frame represented in world frame coordinates.

7.3.4 Base Angular Velocity

Base angular velocity represented in the base frame.

7.3.5 Base Acceleration

Base acceleration represented in the base frame.

7.3.6 Joint Positions

Joint positions provided by sensors or Mujoco simulation.

7.3.7 Joint Velocities

Joint velocities provided by sensors or Mujoco simulation.

7.3.8 Contact Forces

Contact forces provided by sensors or Mujoco simulation.

7.3.9 Base Linear Velocity (Optional)

Base linear velocity represented in the base frame. This is an optional input provided from the Mujoco simulation or external estimator.

7.3.10 Base Linear Position (Optional)

Base linear position represented in the base frame. This is an optional input provided from the Mujoco simulation or external estimator.

7.4 State Estimation

7.4.1 Variables

c_f	:	contacts
x_f	:	foot positions
$\dot{x}_f$	:	foot velocities
x_{hip}	:	hip positions
J	:	Jacobian matrix
$\dot{J}$	:	Jacobian time derivative matrix
p_{com}	:	center of mass position
$\dot{p}_{com}$	:	center of mass velocity

Algorithm 2 State Estimation

Input: Sensors

1: Estimate contacts c_f
2: Calculate Φ_{base} from $\mathbf{q}_{base}$
3: Update kinematics (positional)
4: Calculate J in in W frame
5: Calculate J in in B frame
6: Estimate $\dot{p}_{base}$ (currently using Mujoco sensor)
7: Update kinematics (velocity)
8: Calculate x_f and $\dot{x}_f$ in W frame
9: Calculate x_{hip} in W frame
10: Calculate x_f and $\dot{x}_f$ in B frame
11: Calculate p_{com} and $\dot{p}_{com}$

7.4.2 Contacts

Currently, the contacts are estimated from the contact forces provided by the system inputs.

$$c_f = \begin{cases} 1 \; if \; f_c > 0 \\ 0 \; otherwise \end{cases}$$

7.4.3 Foot Position

Calculated by the dynamics library.

7.4.4 Foot Velocity

Calculated by the dynamics library.

7.4.5 Hip Position w.r.t. the Base

The position of the hip with respect to the base represented in the world frame.

7.4.6 Jacobian

Calculated by the dynamics library.

7.4.7 Jacobian Time Derivative

Calculated by the dynamics library.

7.4.8 Center of Mass Position

Calculated by the dynamics library.

7.4.9 Center of Mass Velocity

Calculated by the dynamics library.

7.5 Walk State

The Walk state machine describes how the system transitions from a standing mode to a walking mode. When a command velocity is greater than zero and the robot is standing, the state machine transitions to a walking state and starts the gait pattern modulator.

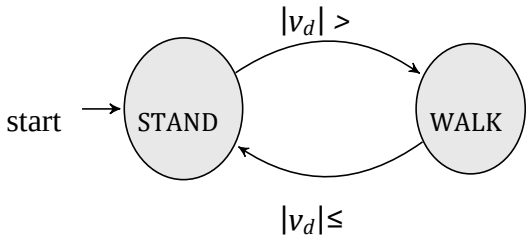

Algorithm 3 STAND State Actions

If $|v_d| > \epsilon$
  Start gait pattern modulator
End if

Algorithm 4 WALK State Actions

If $|v_d| \leq \epsilon$
  Stop gait pattern modulator
End if

7.6 Gait Pattern Modulator

The gait pattern modulator generates the timing and synchronization of the feet for the stance and swing portions of a stride.

7.6.1 Variables

T_{stride}	:	time length of foot stride
T_{st}	:	time length of stance portion of leg stride
T_{sw}	:	time length of swing portion of leg stride
$S_{st,i}$	:	stance state for leg i that maps $[0,T_{st}] \rightarrow [0,1]$
$S_{sw,i}$	:	swing state for leg i that maps $[0,T_{sw}] \rightarrow [0,1]$
S_i	:	stride state for leg i where $S_i = S_{st,i} + S_{sw,i}$
ΔS_i	:	stride state delay for leg i
t_i	:	timer for leg i
φ_i	:	phase lag for leg i

7.6.2 Algorithm

The main algorithm steps are provided in Algorithm (5). First, the gait pattern modulator computes the swing, stance, and full stride times based on the commended velocity and the stride length. Next, the normalized timing signals are updated.

Algorithm 5 Gait Pattern Modulator

Input: L_{span}, $|v_d|$, G_x

Output: S, S_{sw}, S_{st}

Compute stride length

Update S, S_{sw}, and S_{st}

7.6.3 Compute stride length

The swing time is set to a constant value.

$$T_{sw} = 0.25 \text{ (constant)}$$

The stance time is calculated based on the linear part of the command velocity and the stride half length.

$$T_{st} = \frac{2L_{span}}{|v_d|}$$

Finally, the total stride time is computed.

$$T_{stride} = T_{sw} + T_{st}$$

7.6.4 Update S_i, $S_{sw,i}$, and $S_{st,i}$

First, the leg phase lag for each leg is computed based on the gait pattern selected and the total stride time,

$$\varphi_i = \Delta S_i \cdot T_{stride}.$$

Next, each leg timer is updated based on the phase lag,

$$t_i = t + \varphi_i.$$

The current stance state is updated for each leg based on the state of the corresponding leg timer,

$$S_{st,i} = \begin{cases} \frac{t_i}{T_{st}} & 0 \le t_i \le T_{st} \\ 0 & otherwise \end{cases}$$

If the leg timer is within the stance phase of the stride, then $S_{st,i}$ increments from zero to one. With $S_{st,i} = 1$ when $t_i = T_{st}$ and zero when the leg is in a swing phase. The current swing state is updated for each leg base on the state of the corresponding leg timer.

$$S_{st,i} = \begin{cases} \frac{t_i - T_{st}}{T_{sw}} & T_{st} \le t_i \le T_{stride} \\ 0 & otherwise \end{cases}$$

If the leg timer is within the swing phase of the stride, then $S_{st,i}$ increments from zero to one. With $S_{sw,i} = 1$ when $t_i = T_{stride}$ and zero when the leg is in a stance phase. Finally, the current stride state is update by,

$$S_i = S_{st,i} + S_{sw,i}.$$

7.7 Leg State

The leg state machine controls the transitions to and from a stance and swing phase of a stride.

7.7.1 Variables

e_{st} : swing to stance transition event

e_{sw} : stance to swing transition event

c_{sync} : synchronous contact variable

7.7.2 State machine

On boot up, the state machine starts in the 'INIT' state until the system has determined which state (SWING or STANCE) the robot currently is in for each leg. This should occur from contact estimates or sensing, but currently, the system stays in an 'INIT' state until a command velocity greater than zero is desired. Once a command velocity greater than zero is given, the transitions between 'STANCE' and 'SWING' are determined based on the current swing and stance states, $S_{sw,i}$ and $S_{st,i}$, provided by the gait pattern modulator.

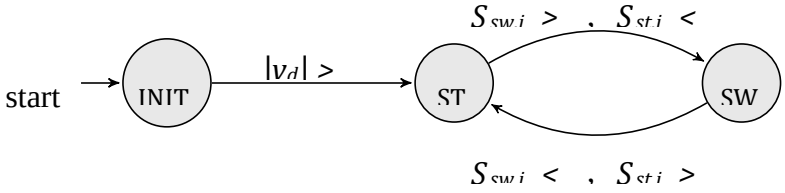

Algorithm 6 STANCE State Actions

If $S_{sw,i} > \epsilon$ and $S_{st,i} < \epsilon$ then

$e_{st} = 0$

$e_{sw} = 1$

$c_{sync} = 0$

end if

Algorithm 7 SWING State Actions

If $S_{sw,i} < \epsilon$ and $S_{st,i} > \epsilon$ then

$e_{st} = 1$

$e_{sw} = 0$

$c_{sync} = 1$

end if

The leg state machine produces events, e_{st} and e_{sw}, on state transitions. The events produced act as signals to the rest of the algorithm indicating when stance phase transitions occur. In addition, the leg state machine provides a variable, c_{sync}, that indicates the current stride phase state. The transition actions taken by the state machine in the 'STANCE' state are given in Algorithm 6). The transition actions taken by the state machine when transitioning to the 'SWING' state are given in Algorithm (7).

7.8 Desired Foot Placement

The desired foot placement is the foot position on the ground where the foot should land at the end of the swing phase. It is calculated at the beginning of a swing phase.

7.8.1 Variables

$p_{ref,i}$: hip position projected on the x-y plane for leg *i*

$p_{des,i}$: desired foot landing position for leg *i*

7.8.2 Algorithm

Algorithm (8) describes the algorithm for calculating the desired foot position. When the robot is in a walking state and a start swing phase event occurs, the desired foot position is computed for the corresponding leg using the position on the floor underneath the hip, the velocity of the center-ofmass, and the stride time. When the robot is in a standing state, the desired foot position is set to the position on the floor underneath the hip of the corresponding leg.

Algorithm 8 Calculate $p_{des,i}$

If WALK is true then

If e_{sw} is 1 then

$p_{des,i} \leftarrow p_{ref,i} + \dot{p}_{com} \cdot \frac{stride}{2} T$

end if

else

$p_{des,i} \leftarrow p_{ref,i}$

end if

7.9 Base Trajectory Generation

The base trajectory is generated for the specified horizon length of the MPC algorithm. The trajectory is computed using the current state of the robot and the desired command velocity, v_d.

7.10 Stance Leg Trajectory

The stance leg trajectory generates a vector from the center-of-mass of the base to the foot position on the ground in the world frame. The trajectory is generated for the specified horizon length.

7.11 Swing Leg Trajectory

The swing leg trajectory is generated using cubic splines. The coefficients of the cubic splines are calculated using the current foot position estimate, desired foot placement, desired swing height, and desired stride length. The swing trajectory is generated in the base frame.

7.11.1 Variables

$p_{dessw,i}$: desired swing foot position for leg *i*

$v_{sw,ides}$: desired swing foot velocity for leg *i*

$a_{dessw,i}$: desired swing foot acceleration for leg *i*

7.11.2 Algorithm

Trajectories are generated using cubic splines. The full algorithm is described in Algorithm (9). The algorithm runs when the robot is in a 'WALKING' state. Coefficients are only calculated when the start of swing phase event occurs. When the phase of the stride is indicated to be in a swing phase, the swing trajectory is updated based on the current swing state, $S_{sw,i}$.

Algorithm 9 Calculate $p_{sw,i}^{des}$ $v_{sw,i}^{des}$ $a_{sw,i}^{des}$

```
if WALK is true then
    if e_sw = 1 then
        Calculate B_pdes,i, B_Hsw, B_xf
        Calculate cubic spline coefficients
    end if
    if c_sync is true then
        Update p_sw,i^des, v_sw,i^des, a_sw,i^des using S_sw,i
    end if
end if
```

7.11.3 Cubic Spline

To calculate the cubic spline coefficients, the desired foot placement, the desired swing height, and the current foot position is transformed into the base frame. The desired foot placement is described in the base frame by

$$B_{p_{des,i}} = B_{R_W}\left(W_{p_{des,i}} - W_{p_{base}}\right)$$

The desired swing height is described in the base frame by,

$${}^{\mathcal{B}}H_{sw} = {}^{\mathcal{B}}R_{\mathcal{W}}{}^{\mathcal{W}}\begin{bmatrix} 0 \\ 0 \\ H_{sw} \end{bmatrix}$$

The current foot position is described in the base frame by

$$B_{x_f} = B_{R_W} W_{x_f}$$

In general, the coefficients of a cubic spline can be calculated by the following linear equation,

$$C_{spline}(p_0,\ p_T,\ v_0,\ v_T,\ T) = \begin{bmatrix} c^{(0)} \\ c^{(1)} \\ c^{(2)} \\ c^{(3)} \end{bmatrix} = \begin{bmatrix} 0 & 0 & 0 & 1 \\ T^3 & T^2 & T & 1 \\ 0 & 0 & 1 & 0 \\ 3T^2 & 2T & 1 & 0 \end{bmatrix}^{-1} \begin{bmatrix} p_0 \\ p_T \\ v_0 \\ v_T \end{bmatrix},$$

where p_0 and p_T are the start and final positions, v_0 and v_T are the start and final velocities, and T is the time duration of the trajectory. In our case, we generate a cubic spline for the x, y, and z directions. The coefficients for the x direction are given by,

$$c_{i,x} = C_{spline}(p_{0,x},\ p_{1,x},\ 0,\ 0,\ 1).$$

where,

$$p_{0,x} = \text{B}x_{fi,x},$$

and,

$$p_{1,x} = \text{B}p_{des,ix}.$$

For the y direction, coefficients are given by,

$$c_{i,y} = C_{spline}(p_{0,x},\ p_{1,x},\ 0,\ 0,\ 1),$$

where,

$$p_{0,y} = \text{B}x_{fi,y},$$

and,

$$p_{1,y} = \text{B}p_{des,iy}.$$

For the z direction, we have two sections of cubic spline, one for moving from the floor to the maximum height and the other moving from the maximum to to the floor. The coefficients for the first half of the z trajectory are,

$$c_{i,z1} = C_{spline}(p_{0,z},\ p_{0.5,z},\ 0,\ 0,\ 0.5),$$

where,

$$p_{0,z} = \text{B}x_{fi,z},$$

and,

$$p_{0.5,z} = \text{B}H_{sw}.$$

For the second half, the coefficients are,

$$c_{i,z2} = C_{spline}(p_{0.5,z},\ p_{1,z},\ 0,\ 0,\ 0.5),$$

where,

$$p_{0.5,z} = \text{B}H_{sw},$$

and,

$$p_{1,y} = \text{B}p_{des,iz}.$$

Now the trajectory in the *x* direction for position can be found for the current time step by,

$$p_{dessw,i,x} = c_{(0)i,x}S_{sw,i3} + c_{(1)i,x}S_{sw,i2} + c_{(2)i,x}S_{sw,i} + c_{(3)i,x}.$$

For the *y* direction, the position trajectory is given by,

$$p_{sw,i,y}^{des} = c_{i,y}^{(0)}S_{sw,i}^3 + c_{i,y}^{(1)}S_{sw,i}^2 + c_{i,y}^{(2)}S_{sw,i} + c_{i,y}^{(3)}.$$

For the *z* direction, the position trajectory is given by,

$$p_{sw,i,z}^{des} = \begin{cases} c_{i,z_1}^{(0)}S_{sw,i}^3 + c_{i,z_1}^{(1)}S_{sw,i}^2 + c_{i,z_1}^{(2)}S_{sw,i} + c_{i,z_1}^{(3)}, & S_{sw,i} \leq 0.5 \\ c_{i,z_2}^{(0)}S_{sw,i}^3 + c_{i,z_2}^{(1)}S_{sw,i}^2 + c_{i,z_2}^{(2)}S_{sw,i} + c_{i,z_2}^{(3)}, & S_{sw,i} > 0.5 \end{cases}.$$

For the *x* direction, the velocity trajectory is given by,

$$v_{sw,i,xdes} = 3c_{(0)i,x}S_{sw,i2} + 2c_{(1)i,x}S_{sw,i} + c_{(2)i,x}.$$

For the *y* direction, the velocity trajectory is given by,

$$v_{sw,i,ydes} = 3c_{(0)i,y}S_{sw,i2} + 2c_{(1)i,y}S_{sw,i} + c_{(2)i,y}$$

For the *z* direction, the velocity trajectory is given by,

$$v_{sw,i,z}^{des} = \begin{cases} 3c_{i,z_1}^{(0)}S_{sw,i}^2 + 2c_{i,z_1}^{(1)}S_{sw,i} + c_{i,z_2}^{(2)}, & S_{sw,i} \leq 0.5 \\ 3c_{i,z_2}^{(0)}S_{sw,i}^2 + 2c_{i,z_2}^{(1)}S_{sw,i} + c_{i,z_2}^{(2)}, & S_{sw,i} > 0.5 \end{cases}$$

For the *x* direction, the acceleration trajectory is given by,

$$a_{dessw,i,x} = 6c_{(0)i,x}S_{sw,i} + 2c_{(1)i,x}$$

For the *y* direction, the acceleration trajectory is given by,

$$a_{sw,i,y}^{des} = 6c_{i,y}^{(0)}S_{sw,i} + 2c_{i,y}^{(1)}$$

For the *z* direction, the acceleration trajectory is given by,

$$a_{sw,i,z}^{des} = \begin{cases} 6c_{i,z_1}^{(0)}S_{sw,i} + 2c_{i,z_1}^{(1)}, & S_{sw,i} \leq 0.5 \\ 6c_{i,z_2}^{(0)}S_{sw,i} + 2c_{i,z_2}^{(1)}, & S_{sw,i} > 0.5 \end{cases}$$

7.12 Stance Leg Control

The stance leg control runs the MPC algorithm to generate linear contact forces that are converted to joint torques using the contact jacobian *J*. The algorithm details are found elsewhere.[7]

7.13 Swing Leg Control

The swing leg controller combines inverse dynamics with PID control to track the swing leg trajectory. The inverse dynamics uses the desired foot acceleration trajectory and measured joint positions and velocities to predict the current joint torques. The PID portion of the control is used to correct for model errors and disturbances, as well as generating the desired dynamic response. The algorithm details are found elsewhere.[7]

8.0 Quadruped Simulation

The previous three sections covered the development of individual elements of the quadruped system simulation. The next step was to integrate these components with the commercial kinematics simulation package MuJoCo to create a cross-platform simulation of the full quadruped, from locomotion control to the hydraulic powertrain to the movement of the robot. This involved linking the associated inputs and outputs of each individual element to transfer the required information, along with any required transformation. For example, the hydraulic model is derived to use linear position and speed of the actuator as an input, but the MPC controls joint position in an angular domain; thus, a transformation from joint angle to actuator position is required to connect the MPC and the hydraulics model.

8.1 System Overview

The primary input into the system is the twist velocity, v_{twist}, which is a 6-dimensional velocity vector that defines the desired robot trunk orientation. This velocity command is passed to the MPC locomotion stack, which calculates an array of joint torque commands, τ_{des}, to manipulate the legs. The sum effects of these torques on the hydraulic fluid supply along the predictive horizon are estimated and passed to the powertrain control block in conjunction with a desired operating fluid pressure, P_{des}, to control the speed, N, of the motor driving the hydraulic pump by commanding a nominal motor voltage, V. The hydraulics model receives these inputs, along with a matrix of join positions and velocities, as well as an array of servo valve commands, i_{des}, that is calculated using a PID control loop on the actuator force. The hydraulics model then calculates the actual motor speed, system pressure, and actuator force. The array of actuator forces is passed through a transform back into joint space where it is output to MuJoCo, which calculates the actual joint positions, q, and its first two derivatives. These are then passed to the MPC to calculate the next iteration. Figure 8-1 shows a block diagram of the integrated simulation system.

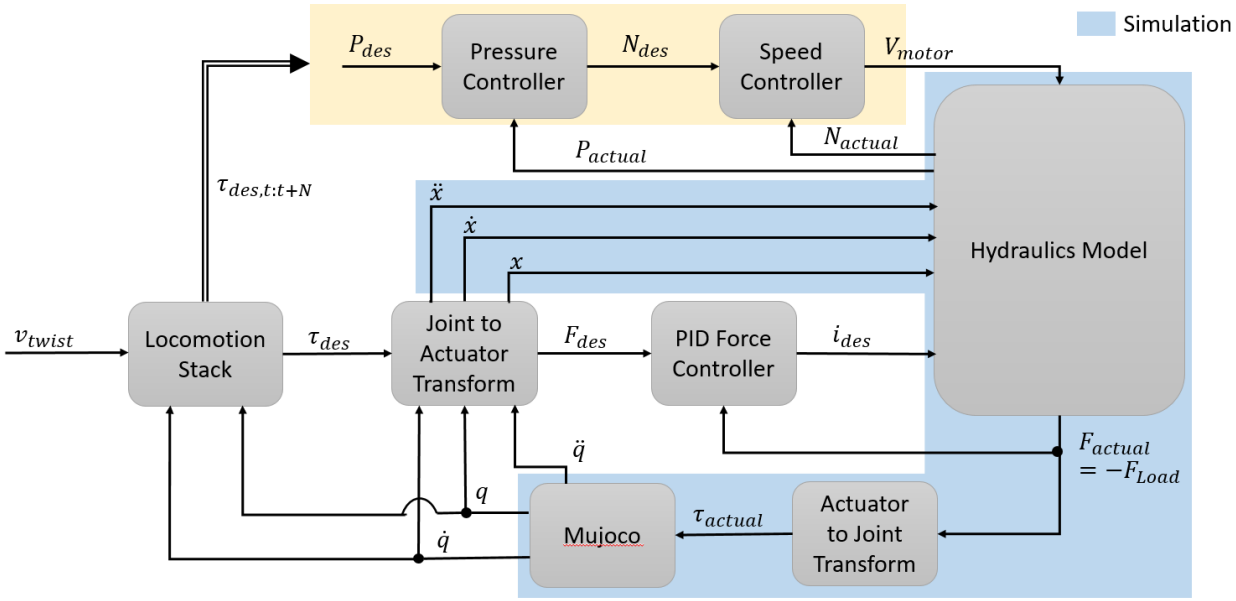

Figure 8-1. Integrated MPC-based locomotion controller, hydraulics model, and multi-body dynamics Mujoco simulation. The Locomotion Stack block refers to the MPC algorithm in Section 7.0.

8.2 Compilation Efforts

The first attempt at system integration involved manual translation of the Hydraulics model in Section 6.0 to C++. In this configuration, the C++ hydraulics model is called by the Mujoco simulation to update the actuator dynamics/forces. This corresponds to the light blue region in Figure 8-1. It was at this point that the need for a stiff solver was discovered, which MuJoCo does not have. System dynamics is generally modeled as a series of differential equations that defines the incremental change in state as a function of current state and applied commands. Behavior of the system over time is then determined through integration of these differential equations. MuJoCo utilizes a standard integrator that integrates the system along fixed time steps, which is generally sufficient for multi-body kinematics as it is considered a slow system. However, hydraulic systems are commonly considered a fast or "stiff" system, where large changes in state can occur across very small time steps. However, integrating the entire simulation time span using such small time steps is very expensive computationally. As such, stiff solvers utilize a variable time step integration that can reduce the time step during periods of high activity and increase the time step during periods of minimal activity. This reduces computational cost while preserving model fidelity. In this application, the problem is that the hydraulic model was developed in Matlab Simulink, which contains multiple stiff solvers, whereas MuJoCo does not have that capability. As such another method of compilation was required.

The next method attempted involved co-simulation of the hydraulics model in Simulink in parallel with the kinematics simulation in MuJoCo. This method involves integrating the MPC-based locomotion controller and the multi-body dynamics MuJoCo simulation into Simulink through S-function interfaces. Simulink then integrates the hydraulic model using a stiff solver and then calls the locomotion controller and MuJoCo simulator at appropriate time steps. It was quickly learned that this method was unacceptable as well since the state evolution within MuJoCo was held constant during the co-simulation process. This basically handcuffed the stiff solver and we therefore were unable to simulate the full system.

The final effort was to disable the numerical integration within MuJoCo and to extract its velocities needing integration and passing them to Simulink to then integrate with the stiff solver. A proof of concept effort successfully accomplished this with a non-stiff test system when using the Euler (fixed time step) integrator. However, it became apparent that MuJoCo performs other special calculations when using multi-step stiff integrators. Since MuJoCo does not have variable time step capacity, this means these calculations assume an incorrect time step, resulting in an inaccurate simulation of the system.

8.3 Future Work

The two stable versions of the simulation, the C++ formulation and the co-simulation between MuJoCo and Simulink, are both capable of simulating the system dynamics when leveraged with a fixed time step integrator across the whole system. However, this requires a very small time step to accurately capture the hydraulic system dynamics, which results in an excessively long computation time. It is estimated that for a single core PC system of the type commonly used at NRL, a 1 second simulation would require 17 hours to complete. In theory machine learning could be used to create an approximation function to mimic the hydraulic system dynamics with larger time steps. However, this still requires training the algorithm to properly capture a sufficient degree of the system behavior, which would still require considerable simulation time.

The primary path forward both requires modification to current commercial rigid-body kinematic simulation software. Two possible avenues exist, the first of which is a kinematics simulation package that is capable of using variable time step (i.e. stiff) solvers. This would eliminate the problem entirely

and facilitate rapid simulation of the system with minimal modification. This could also be achieved by developing a rigid-body kinematics simulation package internally, though that is outside the scope of this project. The other option would be for the kinematics package to allow multi-core processing to enable use of high-power computing clusters for faster computation. However, it is not known if this would require modifications to the other elements within the simulation system as well.

9.0 Conclusion

A combination of the COVID-19 pandemic and technical limitations with commercial kinematics simulation software has meant that the ARTHuR program was unable to achieve the stated goals of the project. However, the work conducted has yielded several lessons learned that can serve to shape future research into this field. In addition, some of this work has already been transitioned to another program to further efforts in quadruped control.

9.1 Lessons Learned

- Current additive manufacturing techniques in stainless steel has not yet achieved the precision required to fabricate components with internal passages with the sufficient precision and consistency that is required for small-scale rotary servo valves. Systems larger than the Butch quadruped (10 kg) with larger servo valves may be possible with existing capabilities.
- Additively manufactured internal passages will be more consistent in shape if they utilize apex angles less than 50°, and preferably less than 40°. This will usually result in unorthodox passage cross section shapes and care must be taken to ensure that the orifice area as a function of spool position is as linear as possible.
- Total system simulation when hydraulic components are present requires the capability for variable time step integration (i.e. stiff solvers) in order to achieve solutions within a feasible time span. If no commercial package is available with that feature, developing a custom rigid-body kinematics modeling package should be considered an integral part of the effort. This limitation is likely not an issue for pneumatic systems, as gas compressibility reduces the stiffness of the system.

9.2 Transitions

The MPC algorithm developed for ARTHuR has been transitioned to the ONR funded program NEMO for use in control of a Ghost Robotics Vision 60 quadruped to develop robotic onboard ship maintenance capabilities.

10.0 References

[1] Manring, Noah D., *Hydraulic Control Systems*, John Wiley and Sons, 2005, pg. 180-186.

[2] Merrit, Herbert E., *Hydraulic Control Systems*, John Wiley and Sons, 1967, pg. 101-103.

[3] Williams, L., "Performance And Selection of Brushless DC Motors for Miniature Hydraulic Powertrains," Proceedings of the 2020 Bath/ASME Symposium on Fluid Power and Motion Control, September 9-11, University of Bath, Bath, UK, 2020.

[4] Williams, L., "Methodology for the Evaluation of Gear Pump Performance," Proceedings of the 2020 Bath/ASME Symposium on Fluid Power and Motion Control, September 9-11, University of Bath, Bath, UK, 2020.

[5] Williams, L., "Dynamic Performance Model of the Single Actuator Testbed," NCST-TP-MER006, 20 November 2015.

[6] Williams, L. and Geating J., "Merlin Hydraulic Power Unit," NCST-TP-MER010, 20 September 2019.

[7] Carlo, J., Wensing, P., Katz, B., Bledt, G., and Kim, S., "Dynamic locomotion in the MIT cheetah 3 through convex model-predictive control," *2018 IEEE/RSJ International Conference on Intelligent Robots and Systems (IROS)*, pp. 1–9, 2018.